



Impact of hydrodynamic dispersion on mixing-induced reactions under radial flows

Pratyaksh Karan, Uddipta Ghosh, Yves Méheust, Tanguy Le Borgne

► To cite this version:

Pratyaksh Karan, Uddipta Ghosh, Yves Méheust, Tanguy Le Borgne. Impact of hydrodynamic dispersion on mixing-induced reactions under radial flows. *Advances in Water Resources*, 2023, 179, pp.104521. <10.1016/j.advwatres.2023.104521>. <insu-04185643>

HAL Id: insu-04185643

<https://insu.hal.science/insu-04185643v1>

Submitted on 23 Aug 2023

HAL is a multi-disciplinary open access archive for the deposit and dissemination of scientific research documents, whether they are published or not. The documents may come from teaching and research institutions in France or abroad, or from public or private research centers.

L'archive ouverte pluridisciplinaire **HAL**, est destinée au dépôt et à la diffusion de documents scientifiques de niveau recherche, publiés ou non, émanant des établissements d'enseignement et de recherche français ou étrangers, des laboratoires publics ou privés.



HAL Authorization

Journal Pre-proof

Impact of hydrodynamic dispersion on mixing-induced reactions under radial flows

Pratyaksh Karan, Uddipta Ghosh, Yves Méheust, Tanguy Le Borgne

PII: S0309-1708(23)00155-0

DOI: <https://doi.org/10.1016/j.advwatres.2023.104521>

Reference: ADWR 104521

To appear in: *Advances in Water Resources*

Received date: 3 May 2023

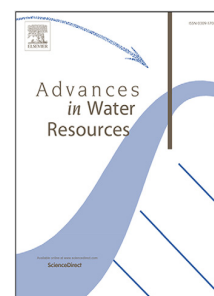
Revised date: 12 August 2023

Accepted date: 15 August 2023

Please cite this article as: P. Karan, U. Ghosh, Y. Méheust et al., Impact of hydrodynamic dispersion on mixing-induced reactions under radial flows. *Advances in Water Resources* (2023), doi: <https://doi.org/10.1016/j.advwatres.2023.104521>.

This is a PDF file of an article that has undergone enhancements after acceptance, such as the addition of a cover page and metadata, and formatting for readability, but it is not yet the definitive version of record. This version will undergo additional copyediting, typesetting and review before it is published in its final form, but we are providing this version to give early visibility of the article. Please note that, during the production process, errors may be discovered which could affect the content, and all legal disclaimers that apply to the journal pertain.

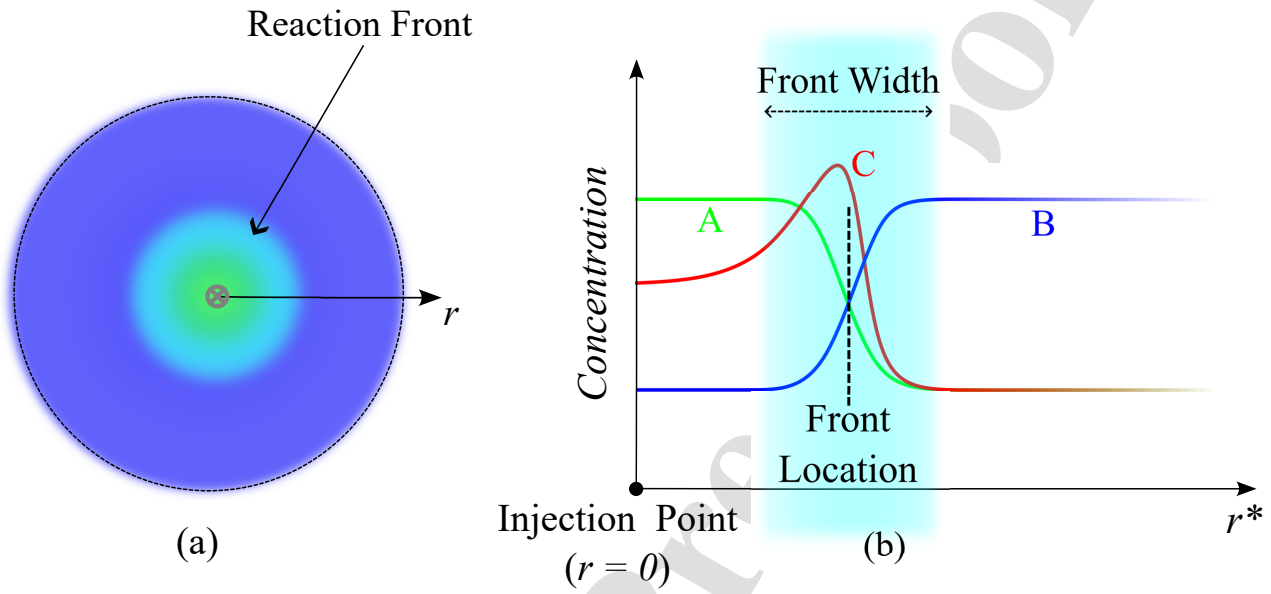
© 2023 Elsevier Ltd. All rights reserved.



Graphical Abstract

Impact of hydrodynamic dispersion on mixing-induced reactions under radial flows

Pratyaksh Karan, Uddipta Ghosh, Yves Méheust, Tanguy Le Borgne



Highlights

Impact of hydrodynamic dispersion on mixing-induced reactions under radial flows

Pratyaksh Karan, Uddipta Ghosh, Yves Méheust, Tanguy Le Borgne

- We study the impact of mechanical dispersion on radially-advected reaction fronts
- We derive scaling laws for the front position and effective reaction rate
- We find that dispersion accelerates the advancement of the front and enhances reaction rates
- We discuss the implications for field applications over a range of temporal and spatial scales

Impact of hydrodynamic dispersion on mixing-induced reactions under radial flows

Pratyaksh Karan^a, Uddipta Ghosh^a, Yves Méheust^b, Tanguy Le Borgne^b

^a*Discipline of Mechanical Engineering, Indian Institute of Technology Gandhinagar, Palaj, Gandhinagar, 382055, Gujarat, India*

^b*Université de Rennes 1, CNRS, Géosciences Rennes, UMR 6118, Rennes, 35042, Brittany, France*

Abstract

Mixing-induced reaction fronts play a key role in a range of subsurface processes. In many applications, reactive fronts develop under radial flows, where a reactant is injected and displaces another. Analytical solutions for reactive front dynamics under radial flows have been derived under the assumption of a constant diffusion coefficient. However, the impact of mechanical dispersion still remains unexplored. We investigate this question here by deriving approximate analytical expressions for the reaction front properties as a function of time, dispersion length and Péclet/Damköhler number, as well as from corresponding numerical simulations. Our results indicate that mechanical dispersion leads to a more advanced front and enhanced reaction rate, compared to the dispersion-free scenario. This leads to new scaling laws for the front position, width and reaction rate. We discuss the implications of these findings for field conditions over a range of temporal and spatial scales. Under most realistic scenarios, dispersion is expected to be dominant over diffusion, suggesting a broad relevance of these results.

Keywords: Radial flow, Mixing-limited reaction, Hydrodynamic Dispersion

1. Introduction

Reactive fronts formed at the interface between two reactive fluids, one of which displaces the other, are ubiquitous in subsurface hydrology, and are relevant to a wide range of processes (Dentz et al., 2011; Rolle and Le Borgne, 2019; Valocchi et al., 2019), including contaminant remediation (Sprocati and Rolle, 2020), aquifer recharge (Maliva and Maliva, 2020; Stolze and Rolle, 2022), CO₂ sequestration (Gautam and Narayana, 2019; Addassi et al., 2022) and geothermal systems

Email addresses: pratyakshkaran@gmail.com (Pratyaksh Karan), uddipta.ghosh@iitgn.ac.in (Uddipta Ghosh), yves.meheust@univ-rennes1.fr (Yves Méheust), tanguy.le-borgne@univ-rennes1.fr (Tanguy Le Borgne)

(Burté et al., 2019). For instance, during in-situ decontamination of soil or groundwater, plumes of bio-chemical reactants are often injected into the subsurface using boreholes, which leads to the formation of moving fronts between the resident species and the injected agent, wherein chemical reactions take place. In the presence of heterogeneous flow fields, these fronts undergo continuous stretching and folding, which enhances mixing by augmenting the local concentration gradients, therefore resulting in increased reaction rates (Dentz et al., 2011; De Anna et al., 2014; Le Borgne et al., 2014, 2015; Jiménez-Martínez et al., 2015; Bandopadhyay et al., 2017; Ghosh et al., 2018). Reactive fronts under radial flows are particularly important as they represent useful models for a number of geologically relevant processes such as contaminant remediation (Neupauer et al., 2020), soil leaching (Batarseh and Stiller, 1994), aquifer recharge (Eldor and Dagan, 1972), where reagent injection takes place over a large vertical segment of a borehole so that dominantly radial flow advects the reaction's reagents and the products.

The dynamics of reactive fronts is often studied by considering bimolecular $A + B \rightarrow C$ type reactions (Gálfi and Rácz, 1988; Larralde et al., 1992; Brau et al., 2017; Bandopadhyay et al., 2017; Comolli et al., 2019; Budroni et al., 2019; Brau and De Wit, 2020; Comolli et al., 2021; Guilbert et al., 2021). They represent simple models for a wide spectrum of mixing-induced reactions such as precipitation (Luo et al., 2008; Edery et al., 2009; Arshadi and Rajaram, 2019), contaminant degradation (Wing, 1997; Miller et al., 1998; Copley, 2009) and redox processes (Liu et al., 2016; Burté et al., 2019; Bochet et al., 2020), to underline a few. The kinetics of such bimolecular reactions in radial flows have so far been studied at the continuum/Darcy scale under the assumption of a constant diffusion coefficient (Brau et al., 2017; Bandopadhyay et al., 2017; Comolli et al., 2019; Brau and De Wit, 2020), which uncovered the various regimes and scaling laws for effective reaction rates. However, a complete continuum/Darcy scale description of reactive transport in porous media should account for *hydrodynamic* (also, *mechanical*) dispersion.

In many applications, hydrodynamic dispersion, rather than molecular diffusion, is expected to dominate the continuum scale dynamics of transport in porous media (Saffman, 1959; Levy and Berkowitz, 2003; Dentz et al., 2011; De Anna et al., 2013; Noetinger et al., 2016; Bear, 2018; Wang et al., 2020; Neupauer et al., 2020). At the pore-scale, the transport phenomena is characterized by heterogeneous advection borne out of the local variations in the flow passages and the velocity field. The pore-scale coupling of the heterogeneity in advection and molecular diffusion manifests at the Darcy scale as mechanical dispersion, which is usually modelled as a Fickian transport mechanism

with a flux proportional to the local upscaled concentration gradient and the averaged velocity (Bear, 2018). The upscaled reactive transport at the Darcy scale is consequently encapsulated in the advection-dispersion-reaction equation (ADRE) (Dentz et al., 2011; Bear, 2018). While this representation is broadly used to study reactive transport problems, it does not capture anomalous (i.e., non-Fickian) transport dynamics inherent to moderate to strongly heterogeneous media (Berkowitz et al., 2006; Neuman and Tartakovsky, 2009). For reactive fronts under radial flows, however, the question of how Fickian dispersion couples with the resulting non-uniform flow to govern reaction laws remains as yet unexplored.

In this study, we analyze the impact of hydrodynamic dispersion on a radially moving bimolecular $A+B \rightarrow C$ type reaction front, wherein species ‘B’ is displaced by continually injecting species ‘A’ into a porous medium with uniform permeability. We present both numerical solutions to the pertinent governing equations, as well as analytical approximations of these solutions. Our results indicate that mixing in the reaction front is initially dominated by dispersion, which qualitatively impacts the front’s properties, including its position, width, and global reaction rate. We derive the corresponding scaling laws, which differ from those known for diffusion-dominated regimes.

The article is arranged as follows. In §2, we present the physical description of the system along with the governing equations and the boundary conditions. §3 discusses the approximate analytical solutions for the various front properties along with the results emerging out of our analysis. We conclude in §4. It is followed by §Appendix A, where a brief overview of the numerical solution methodology is outlined, and §Appendix B and §Appendix C, where details of the analytical solutions are provided.

2. The governing equations for reactive transport

2.1. Physical description of the system under consideration

We consider an ambient solution residing in a porous domain of uniform permeability (K) with uniform porosity (ϕ_0), wherein the reactant species B is dissolved with a uniform initial concentration c_0 . A solution of the reactant species ‘A’ with the same uniform concentration (c_0) is introduced into the porous media through a flux-averaged line injection on the vertical axis of the reference frame, with a constant volumetric flow rate ($2\pi Q_0$) per unit depth. As the fluid containing solute ‘A’ invades the porous media, a circular reaction front develops between the species ‘A’ and ‘B’ where a third species ‘C’ is produced, as depicted in figure 1. Due to the

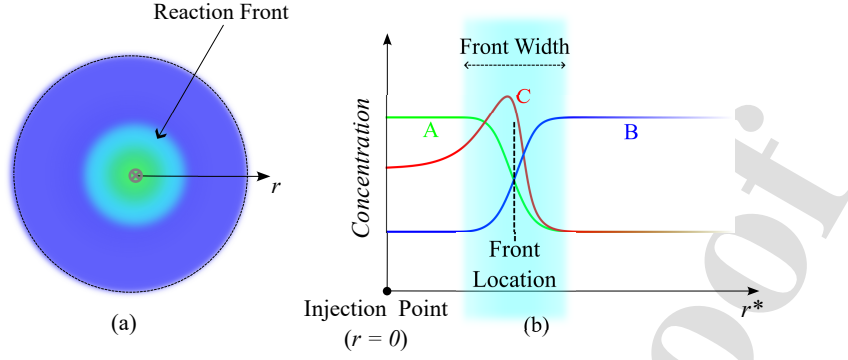


Figure 1: Illustrative representation of a cylindrical reaction front; the plot cartoon in (b) demonstrates a typical reaction front and the typical concentration distributions for the reactants (A and B) and the product (C) in its vicinity.

continuous injection of ‘A’ at the origin, the circular (axisymmetric) front is advected radially outward. We shall assume the rate of reaction between ‘A’ and ‘B’ to follow a first order kinetics given by, $R'(\mathbf{x}', t') = k_R c'_A(\mathbf{x}', t') c'_B(\mathbf{x}', t')$, where $R'(\mathbf{x}', t')$ is the rate of reaction, $c'_i(\mathbf{x}', t')$ ’s are the concentrations of solute ‘i’ (which represents A, B or, C) at position \mathbf{x}' and time t' and k_R is the reaction rate constant, all evaluated at the Darcy scale. The stoichiometric coefficients of all the species involved in the reaction are taken to be identical. We also assume that the effect of small scale porous media heterogeneity is encapsulated in the dispersion coefficient. In future studies, the effect of macroscopic heterogeneities may be investigated by considering heterogeneous permeability fields. This would lead to stretching of the reaction fronts and thus to enhanced mixing and reaction (Le Borgne et al., 2014). In what follows, we shall further assume that the Reynolds number (Re) at the pore scale remains sufficiently small (quantified ahead in §3.3) so that the linear (Darcian) relation between the discharge rate and the hydraulic head is maintained and the flow does not spontaneously become non-axisymmetric.

2.2. The hydrodynamic dispersion tensor

For flows through porous media, the transport of a dissolved species (say, species i) is governed by the advection-dispersion-reaction equation (ADRE), expressed as (Dentz et al., 2011; Bear, 2018):

$$\frac{\partial c'_i}{\partial t'} + \mathbf{v}' \cdot \nabla c'_i = \nabla' \cdot (\mathbf{D}^* \cdot \nabla' c'_i) + R'_i, \quad (1)$$

where, c'_i is the Darcy-scale concentration of the dissolved species, t' is the time, \mathbf{v}' is the interstitial velocity (i.e., local fluid velocity averaged over the intersection of the pore space and a representative elementary volume), ∇' is the gradient operator (see the Appendix A in Leal, 2007, for detailed

expressions), R'_i is the local reaction rate per unit volume, defined here as $-c'_A c'_B$ when $i = A$, B and $c'_A c'_B$ when $i = C$, and \mathbf{D}^* is the hydrodynamic dispersion tensor which may be written as (Dentz et al., 2011; Noettinger et al., 2016; Bear, 2018) :

$$\mathbf{D}^* = \mathbf{D}_M^* + \ell_T \|\mathbf{v}'\| \mathbf{I} + (\ell_L - \ell_T) \frac{\mathbf{v}' \mathbf{v}'}{\|\mathbf{v}'\|}, \quad (2)$$

In the above, \mathbf{I} is the identity tensor, ℓ_T and ℓ_L are respectively the transverse and longitudinal mechanical dispersion lengths and \mathbf{D}_M^* is the effective (or, apparent) molecular diffusion coefficient of the solute in porous media (i.e., $\mathbf{D}_M^* = \bar{D}_M \mathbf{T}^*$ where \bar{D}_M is the molecular diffusivity and \mathbf{T}^* is the tortuosity of the porous media), and the argument $\|\cdot\|$ denotes the magnitude of a vector. In this study, we shall assume \mathbf{D}_M^* to be in the form $\mathbf{D}_M^* = D_M \mathbf{I}$, where $\mathbf{T}^* = \lambda \mathbf{I}$ and $D_M = \bar{D}_M \lambda$, which implies isotropic and homogeneous effective (or, apparent) diffusivity, resulting from an isotropic and uniform tortuosity tensor. Note that we have chosen to follow Bear (2018) in defining λ as a scalar in the range $[0; 1]$; the inverse definition (with $\lambda^* \in [1; +\infty[$) is also widespread in the literature, in which case $D_M = \bar{D}_M / \lambda^*$ and the tortuosity factor (λ^*) is interpreted as the squared ratio of a typical streamline's length to the linear size of the medium (Guyon et al., 2015). It may be observed that in the absence of any mechanical dispersion (i.e. when $\ell_L = \ell_T = 0$) or of flow ($\mathbf{v}' = 0$) or both, the dispersion tensor reduces to an isotropic effective diffusion tensor. For the axisymmetric scenario that we investigate here, ℓ_T is found to not contribute to the transport processes.

2.3. The governing equations for the concentrations of A, B and C

We first introduce the non-dimensional versions of the governing equations. To this end, the dimensionless version ψ of any variable, ψ' (which could represent c'_A , \mathbf{x}' , t' , etc.), is written as: $\psi = \frac{\psi'}{\psi_c}$, where ψ_c is the characteristic scale of the said variable. The characteristic scales for all the pertinent variables are listed in table 1. Here we have chosen the reaction time ($t_R \sim 1/k_R c_0$) as the characteristic time scale because it is the only naturally occurring time-scale in the problem. As a consequence, it follows that $t = 1$ demarcates a transition in the reactive transport process; prior to $t = 1$, the reaction is largely limited by the reaction kinetics, which results in a reaction-limited regime as quantified ahead in §3.2.1 and 3.2.2. On the other hand, when $t > 1$, the reaction has progressed sufficiently and most of the reactants would be consumed if they were properly mixed. As a result, the global reaction rate at this stage largely depends on how fast the reactants are mixing, which leads to the mixing-limited regime as quantified ahead in the forthcoming sections.

Table 1: Characteristic scales of the relevant variables.

Variable	Char. Scale	Remarks
Concentration (c_c)	c_0	Injection and resident concentrations of species A and B respectively
Time (t_c)	$(k_R c_0)^{-1}$	Reaction time scale
Coordinate length (r_c)	$\sqrt{(Q_0/\phi_0)/(k_R c_0)}$	Distance traveled by the front at time t_c
Velocity (v_c)	$(Q_0/\phi_0)/r_c$	Averaged characteristic velocity over pore space

Proceeding with the reaction time as the time scale, the volumetric flow rate per unit vertical length ($2\pi Q_0$) and the reactant concentration (c_0), it is possible to define characteristic scales for length, velocity, etc., as shown in Table 1. The length scale is defined from the volumetric flow rate per unit vertical length and the time scale. The characteristic velocity v_c is defined as the velocity at distance r_c from the injection line. We have used cylindrical (polar) coordinates for the subsequent analysis, and because of the axisymmetric nature of the problem, it follows that the velocity field will be of the form,

$$\mathbf{v} = v_r \hat{\mathbf{e}}_r = r^{-1} \hat{\mathbf{e}}_r, \quad (3)$$

(which is purely radial) as mandated by the solvent mass conservation principle. Furthermore, all concentrations will be functions of r and t only.

From these characteristic scales, we can define the dimensionless numbers characterizing the reactive transport problem. The Damköhler number (Da) (Dentz et al., 2011) is defined as the ratio of the diffusion time scale ($t_D = r_c^2/D_M$) to the reaction time scale (t_c)

$$Da = \frac{r_c^2/D_M}{t_c} = \frac{(Q_0/\phi_0)}{D_M}, \quad (4)$$

where we have taken the effective molecular diffusivities (D_M) of all the species to be identical. In this study, since the characteristic spatial scale is also defined based on the reaction time scale, the Damköhler number becomes identical to the Peclet number, which characterizes the ratio of the diffusion time scale to the advection time scale,

$$Pe = \frac{r_c^2/D_M}{r_c/v_c} = \frac{(Q_0/\phi_0)}{D_M}. \quad (5)$$

We thus define the non-dimensional reactive transport equations using the Peclet number henceforth. Note that the usual definition of the Péclet number based on the dispersion length may be

written as: $Pe_s = u' \ell_L / D_M$, where $u' = (Q_0 / \phi_0) / r'$ is the local velocity at r' . Evidently, Pe_s decays in time (or, with r'), which reflects the fact that for the velocity field being studied here (which decays with the radial distance), the front encounters smaller velocities as it progresses to larger radial distances at later times. The non-dimensional numbers Pe in Eq. (5) and Pe_s are related as $Pe_s = Pe(\ell_L / r')$, which indicates that the standard Péclet number and the one defined in Eq. (5) would be equal when the front has travelled a distance $r'_f = \ell_L$. Subsurface flows, especially those prevailing in applications such as aquifer decontamination, typically entail $Pe \geq 1$. Furthermore, the diffusion-dominated cases have already been studied extensively in the literature (Brau et al., 2017; Brau and De Wit, 2020). Therefore, here we shall focus on the cases where $Pe \geq 1$ at the injection.

We also define the dimensionless longitudinal dispersion length η , which essentially characterizes the strength of mechanical dispersion:

$$\eta = \frac{\ell_L}{r_c} = \ell_L \left(\frac{k_R c_0}{Q_0} \right)^{1/2}. \quad (6)$$

By extension, ηPe gives an indication of how strong dispersion is in comparison to diffusion.

Using the characteristic scales defined in Table 1, the non-dimensional version of the ADRE (Eq. (1)) may be expressed in the axisymmetric polar coordinate system as follows:

$$\frac{\partial c_i}{\partial t} + v_r \frac{\partial c_i}{\partial r} = \frac{1}{Pe} (\eta Pe v_r + 1) \frac{1}{r} \frac{\partial}{\partial r} \left(r \frac{\partial c_i}{\partial r} \right) + \eta \frac{\partial v_r}{\partial r} \frac{\partial c_i}{\partial r} + R_i(r, t), \quad (7a)$$

$$R_i(r, t) = \begin{cases} -c_A c_B & \text{when } i = A, B \\ +c_A c_B & \text{when } i = C \end{cases} \quad (7b)$$

Eq. (7a) is subject to the boundary conditions, $c_A = 1$, $c_B = \partial_r c_C = 0$ as $r \rightarrow 0$ and $c_B = 1$, $c_A = \partial_r c_C = 0$ as $r \rightarrow \infty$, and the initial condition, $c_B = 1$, $c_A = c_C = 0$ at $t = 0$, $\forall r$, where ∂_r denotes the partial derivative with respect to r . We may substitute the expression for v_r as mentioned earlier in Eq. (3) into Eq. (7), which then simplifies to (written explicitly for each of the species A, B and C):

$$Pe \frac{\partial c_A}{\partial t} = \left(\frac{\eta Pe}{r} + 1 \right) \frac{\partial^2 c_A}{\partial r^2} + \left(\frac{1 - Pe}{r} \right) \frac{\partial c_A}{\partial r} - Pe c_A c_B, \quad (8a)$$

$$Pe \frac{\partial c_B}{\partial t} = \left(\frac{\eta Pe}{r} + 1 \right) \frac{\partial^2 c_B}{\partial r^2} + \left(\frac{1 - Pe}{r} \right) \frac{\partial c_B}{\partial r} - Pe c_A c_B, \quad (8b)$$

$$Pe \frac{\partial c_C}{\partial t} = \left(\frac{\eta Pe}{r} + 1 \right) \frac{\partial^2 c_C}{\partial r^2} + \left(\frac{1 - Pe}{r} \right) \frac{\partial c_C}{\partial r} + Pe c_A c_B. \quad (8c)$$

3. Results and Discussion

We will now quantify the impact of dispersion, represented by finite values of η , on the front propagation and reaction rates using both numerical and approximate analytical solutions of Eq. (8). Numerical solutions (of Eq. (7)) are computed using an implicit finite difference scheme along with source term linearization to handle the non-linear reaction terms. Further details on the numerical scheme are given in §Appendix A. Approximate analytical solutions to Eq. (8) are discussed ahead in the section.

The dispersion-free scenario corresponding to $\eta = 0$ has been investigated recently by Brau et al. (2017) and Brau and De Wit (2020). As expected, our solutions (both numerical and analytical) for the limiting case $\eta = 0$ agree with the ones reported in those studies. In what follows, we shall first define some of the key properties of the front in §3.1, following which the key inferences from the analytical and numerical solutions will be discussed in §3.2. Finally in §3.3 representative scenarios relevant to subsurface hydrology are outlined, where the findings from this study may be useful.

Although in this article we focus on the case where both the reactants have equal initial concentrations (c_0), numerical simulations with distinct initial reactant concentrations suggest that the essential physics remains unaltered in the latter cases. In particular, the scaling insights and the analytical approximations discussed ahead remain applicable to the reactive transport processes even if the initial concentrations of A and B are different, as verified by the numerical solutions of Eq. (8) and hence for the sake of brevity the results from such cases have not been explicitly included in this article.

3.1. Reactive front metrics

Subtracting Eq. (8b) from Eq. (8a) gives the conservative equation for $\theta = c_A - c_B$ as,

$$Pe \frac{\partial \theta}{\partial t} = \left(\frac{\eta Pe}{r} + 1 \right) \frac{\partial^2 \theta}{\partial r^2} + \left(\frac{1 - Pe}{r} \right) \frac{\partial \theta}{\partial r}. \quad (9)$$

Eq. (9) admits a similarity solution for certain limiting scenarios, as shown later and these will be key to the approximate analytical treatment of the front. However, before proceeding ahead, it is important to first outline the key front properties that we shall focus on.

First, the reaction front location r_f is defined as the location where $\theta = 0$ (or, $c_A = c_B$) (Gálfi and Rácz, 1988), since both c_A and c_B being equal in concentration implies that the reaction is significant at and around this location (c_B is zero for smaller radial locations whereas c_A is zero for larger radial locations). Second, the reaction front's half width w_f (henceforth referred to as

‘width’ for brevity), quantifying the thickness of the region where most of the reaction takes place, is defined from the normalized second moment of the reaction rate field about the reaction front as follows (Gálfi and Rácz, 1988):

$$w_f = \left[\frac{\int_{r \rightarrow 0}^{r \rightarrow \infty} 2\pi r c_{ACB} (r - r_f)^2 dr}{\int_{r \rightarrow 0}^{r \rightarrow \infty} 2\pi r c_{ACB} dr} \right]^{\frac{1}{2}}. \quad (10)$$

Third, the global reaction rate \bar{R} is evaluated by integrating the local reaction rate field ($R = c_{ACB}$) over the entire domain:

$$\bar{R}(t) = 2\pi \int_{r \rightarrow 0}^{r \rightarrow \infty} c_{ACB} r dr. \quad (11)$$

Finally, the mass of the product is computed as the integral of the concentration field over the entire domain

$$M_C(t) = 2\pi \int_{r \rightarrow 0}^{r \rightarrow \infty} c_C r dr. \quad (12)$$

Integrating Eq. (8c) over time ($[0; t]$) and space ($[0; +\infty[$), we observe that the integrals with spatial derivatives as integrands vanish owing to the boundary conditions (see the discussion after Eq. (7)), which directly leads to the following alternative expression for the mass of the product:

$$M_C(t) = \int_0^t dt^* \bar{R}(t^*). \quad (13)$$

3.2. Behavior of the cylindrical reaction front

A few key inferences may be immediately noted from Eqs. (8) and (9), which help steer the forthcoming analysis:

- (i) At early times ($t \ll 1$), the reaction front will reside very close to the injection line such that $r_f \ll 1$, and thus, examining Eqs. (8) and (9) one concludes that close to the front $\eta Pe/r \gg 1$, which indicates that mechanical dispersion will dominate over molecular diffusion during this time period.
- (ii) On the other hand, it may be shown (see the study of the dispersion-free scenario by Brau and De Wit, 2020) that radially advected fronts never reach a steady state (because Eq. (9) does not admit a physically consistent stationary solution). Hence, if allowed to progress, the reaction front will eventually reach a position where that $\eta Pe/r_f \ll 1$, notwithstanding the values of η and Pe . At this stage, the flow velocity (which is $1/r$) is sufficiently small for

$\eta Pe/r$ to become negligible in the factor $(\eta Pe/r + 1)$ appearing in Eq. (9). In other words, molecular diffusion will be dominant over dispersion and the front will essentially behave as one without any dispersion.

- (iii) By combining the observations above, we can deduce that in the presence of dispersion ($\eta \neq 0$), the reaction front will always start in a dispersion-dominated regime at early times ($t \ll 1$) and will eventually transition into a diffusion-dominated (or non-dispersive) regime at large times ($t \gg 1$). Examining Eq. (9), specifically the term $(\eta Pe/r + 1)$ which is the only term that incorporates the effect of dispersion, one observes that the dispersion-dominated regime shall persist whilst $r_f \ll \eta Pe$ and the diffusion-dominated regime will set in when $r_f \gg \eta Pe$, while the transition between the two regimes occurs around $r_f \sim \eta Pe$.

We shall now examine the dispersion-dominated and the diffusion-dominated regimes, respectively in §3.2.1 and §3.2.2. Subsequently, the transitions between the various transport regimes will be ascertained in §3.2.3.

3.2.1. The Dispersion-dominated regime ($r_f \ll \eta Pe$)

As noted in point (iii) above, at early times $r_f \ll \eta Pe$, and thus, in the vicinity of the front, i.e., for $|r - r_f| \lesssim w_f$, Eq. (9) simplifies to,

$$\frac{\partial \theta}{\partial t} = \frac{\eta}{r} \frac{\partial^2 \theta}{\partial r^2} + \left(\frac{1 - Pe}{Pe r} \right) \frac{\partial \theta}{\partial r}. \quad (14)$$

We now seek a similarity solution for θ of the form $\theta = \theta(\xi_{\text{disp}})$, by carrying out the following change of variable, $\xi_{\text{disp}} = r^3/(9\eta t)$, which results in Eq. (14) transforming into:

$$\frac{d^2 \theta}{d\xi_{\text{disp}}^2} + \left[\frac{2}{3\xi_{\text{disp}}} + \frac{1 - Pe}{3\eta Pe} \frac{r}{\xi_{\text{disp}}} + 1 \right] \frac{d\theta}{d\xi_{\text{disp}}} = 0. \quad (15)$$

We note from Eq. (15) that under the condition,

$$r_f \ll \left| \frac{2\eta Pe}{1 - Pe} \right|, \quad (16)$$

the second term in the square braces becomes negligible and then it is possible to derive a similarity solution of the form $\theta(\xi_{\text{disp}})$ to Eq. (15). Now, the above condition is identically satisfied whenever $Pe = 1$, regardless of the value of η . On the other hand, for $Pe \gg 1$, the condition (16) is satisfied when $r_f \ll 2\eta = O(\eta)$. With the second term in the square braces thus dropped, Eq. (15) (or, equivalently, Eq. (14)) naturally admits a similarity solution of the form:

$$\theta = -1 + 2\bar{\Gamma} \left(\frac{1}{3}, \xi_{\text{disp}} \right) = -1 + 2\bar{\Gamma} \left(\frac{1}{3}, \frac{r^3}{9\eta t} \right), \quad (17)$$

where $\bar{\Gamma}(a, x)$ is the normalized gamma function (Olver et al., 2010, see Sec. 8.2.1 on page 174 therein), which is the ratio of the upper incomplete gamma function $\Gamma(a, x)$ and the complete gamma function $\Gamma(a)$, defined as:

$$\bar{\Gamma}(a, x) = \frac{\Gamma(a, x)}{\Gamma(a)}, \text{ where, } \Gamma(a, x) = \int_x^\infty t^{a-1} \exp(-t) dt, \text{ and } \Gamma(a) = \int_0^\infty t^{a-1} \exp(-t) dt. \quad (18)$$

Although Eq. (14) is strictly valid in the vicinity of the front $|r - r_f| < w_f$, its solution in the form as presented in Eq. (17) does satisfy the boundary conditions $\theta(r \rightarrow 0, t) = 1$ and $\theta(r \rightarrow \infty, t) = -1$, and therefore, may be treated as the complete solution as long as $r_f \ll \eta Pe$. Furthermore, the front location is the value of r such that $\theta = 0$:

$$r_f = \mathcal{A}_{\text{disp}} t^{\frac{1}{3}}, \quad \mathcal{A}_{\text{disp}} = (9\eta)^{\frac{1}{3}} \left[\bar{\Gamma}^{-1} \left(\frac{1}{3}, \frac{1}{2} \right) \right]^{\frac{1}{3}}, \quad (19)$$

thus implying $r_f \sim t^{1/3}$ when $\eta \neq 0$. Note that $\bar{\Gamma}^{-1}$ is the inverse normalized gamma function, i.e., if $y = \bar{\Gamma}(a, \tilde{x})$, then $\tilde{x} = \bar{\Gamma}^{-1}(a, y)$.

While Eqs. (17) and (19) provide valuable information on front propagation, further insights into the reaction metrics (i.e., the global reaction rate and the front width) and the product mass may be obtained by approximating the concentration of A as:

$$c_A = t^{-\frac{\beta}{2}} G(z), \quad z = \frac{r - r_f}{t^\alpha}. \quad (20)$$

This expression follows from an ansatz similar to the earlier studies without dispersion (Gálfi and Rácz, 1988; Brau and De Wit, 2020), and is chosen because this particular form enables us to simplify Eq. (8a) into an ODE for $G(z)$. This, as we show later, helps us analyze the state of the reaction at various temporal regimes, while the values of the parameters α and β are linked to the temporal scalings of the front properties. Indeed, we have verified (not shown here for brevity) that Eq. (20) accurately represents the numerical solutions for c_A when the appropriate solution for $G(z)$ is used. In Eq. (20), the term t^α essentially represents the width of the region where c_A (as well as c_B) varies from zero to one, which indicates that the reaction zone width is also expected to scale as t^α . On the other hand, $t^{-\beta/2}$ represents the fact that the reaction front should get depleted of the reactant A (and also B, whose decay rate is also deduced as $t^{-\beta/2}$ in Eq. (B.4)) as time progresses. The variations in the concentrations within the front is captured by the function $G(z)$.

Using the above form of c_A and the Taylor series expansion of the solution for θ from Eq. (17) around the reaction front, Eq. (8a) can be transformed into an ODE governing the function $G(z)$,

whilst also yielding the values of the exponents α and β . The details of this derivation have been included in §Appendix B. We also show in §Appendix B that the global reaction rate takes the following form in the dispersion-dominated regime (see Eq. (B.6)):

$$\bar{R}(t) = 2\pi \int_{-\infty}^{\infty} (G^2 + \mathcal{K}_{\text{disp}} z G) (\mathcal{A}_{\text{disp}} + z t^{\alpha-1/3}) t^{\alpha-\beta+1/3} dz, \quad (21)$$

where $\mathcal{K}_{\text{disp}}$ is a constant derived ahead in §Appendix B.

Depending on whether the dispersion-dominated regime persists for a sufficiently long time (i.e., whether $r_f \ll \eta Pe$ remains true for $t > 1$), it may be further broken down into two distinct sub-regimes. First, at sufficiently small times ($t \ll 1$), the front goes through a *dispersion-dominated reaction-limited* sub-regime, wherein the reaction front metrics show the following variations with time:

$$\bar{R}(t) \sim t^{2/3}; \quad M_C \sim t^{5/3} \quad \text{and} \quad w_f \sim t^{1/3}, \quad (22)$$

see §Appendix B.1 for a detailed derivation.

Second, when ηPe is sufficiently large ($\eta Pe \gg 1$), the front still resides within the dispersion-dominated region even when $t \gg 1$ and this leads to the commencement of the *dispersion-dominated mixing-limited* sub-regime. Further, if $\eta \gg 1$, from the derivation in §Appendix B.2, we infer the following scalings for the reaction front metrics:

$$\bar{R}(t) \sim t^{-1/3}; \quad M_C \sim t^{2/3} \quad \text{and} \quad w_f \sim t^0. \quad (23)$$

Further ahead (see §3.2.3.1), we establish that the scaling laws in Eq. (23) remain valid for the time period $1 < t < t_{\text{tr}}^{\text{disp}}$, where $t_{\text{tr}}^{\text{disp}} \sim \eta^2$. We emphasize that the dispersion-dominated reaction-limited sub-regime at early times always manifests whenever $\eta > 0$, whereas the dispersion-dominated mixing-limited sub-regime only comes into existence when either mechanical dispersion is sufficiently strong or, molecular diffusion is weak (or, both).

3.2.2. The Diffusion-dominated Regime ($r_f \gg \eta Pe$)

If the front is allowed to progress for a sufficiently large amount of time, eventually we must have $r_f \gg \eta Pe$, i.e., at and around the reaction front, molecular diffusion will dominate over mechanical dispersion. Reactive front dynamics in radially advected fronts in the presence of a uniform molecular diffusion coefficient has been investigated in previous studies (Brau et al., 2017; Brau and De Wit, 2020). In the diffusion-dominated regime, the front exhibits the same behavior

as outlined by these studies. We shall thus only briefly discuss the key features of this regime. First, since the front is now at a distance (from the injection line) sufficiently large compared to the region where dispersion is significant (dispersion is non-negligible only for $r \lesssim \eta Pe$), Eq. (9) simplifies to,

$$Pe \frac{\partial \theta}{\partial t} = \frac{\partial^2 \theta}{\partial r^2} + \left(\frac{1 - Pe}{r} \right) \frac{\partial \theta}{\partial r}, \quad (24)$$

which admits a similarity solution for θ :

$$\theta = -1 + 2\bar{\Gamma} \left(\frac{Pe}{2}, \frac{Pe r^2}{4t} \right). \quad (25)$$

The front location is then given by (at the front, $\theta(r_f, t) = 0$),

$$r_f = \mathcal{A}_{\text{diff}} t^{\frac{1}{2}}, \text{ where } \mathcal{A}_{\text{diff}} = \sqrt{\frac{4\bar{\Gamma}^{-1} \left(\frac{Pe}{2}, \frac{1}{2} \right)}{Pe}}, \quad (26)$$

thus implying $r_f \sim t^{1/2}$. For $Pe \gg 1$, $\mathcal{A}_{\text{diff}} \approx \sqrt{2}$ and $r_f \sim \sqrt{2t}$, and thus the front is advected as if attached to a fluid parcel moving with the flow. We reiterate that in the absence of mechanical dispersion (i.e., $\eta = 0$ identically), Eq. (24) remains valid and Eq. (25) represents the solution for θ at all times, as previously shown by Brau et al. (2017).

Further insights into the reaction metrics may be obtained using the same procedure as outlined in §3.2.1 - see §Appendix B for detailed derivation. The global reaction rate may now be written as (see Eq. (B.6)):

$$\bar{R}(t) = 2\pi \int_{-\infty}^{\infty} (G^2 + \mathcal{K}_{\text{diff}} z G) (\mathcal{A}_{\text{diff}} + z t^{\alpha-1/2}) t^{\alpha-\beta+1/2} dz, \quad (27)$$

where $\mathcal{K}_{\text{diff}}$ is a constant, defined ahead in Appendix B.

When mechanical dispersion is sufficiently weak ($\eta \ll 1$), the condition $r_f \gg \eta Pe$ may also be satisfied at early times ($t \ll 1$) and this will result in a *diffusion-dominated reaction-limited* sub-regime. We show in §Appendix B.3 that the reaction metrics during this early time period take the following asymptotic forms:

$$\bar{R}(t) \sim t; \quad M_C \sim t^2 \quad \text{and} \quad w_f \sim t^{1/2}. \quad (28)$$

Conversely, at sufficiently large times ($t \gg 1$), the condition $r_f \gg \eta Pe$ must be satisfied, regardless of how strong mechanical dispersion is. This corresponds to the *diffusion-dominated mixing-limited* sub-regime, wherein the following reaction metrics are observed:

$$\bar{R}(t) \sim t^0; \quad M_C \sim t \quad \text{and} \quad w_f \sim t^{1/6}, \quad (29)$$

as shown by Brau et al. (2017) (also see §Appendix B.4 for a derivation).

We reemphasize that the diffusion-dominated mixing-limited sub-regime will always manifest regardless of how strong dispersion is, provided that the front is allowed to move for a sufficiently long time. On the other hand, the early time diffusion-dominated reaction-limited sub-regime is only realized when mechanical dispersion is very weak, which results in the front transitioning out of the dispersion-dominated region while the reaction is still in the kinetics limited regime ($t \ll 1$).

A summary of the expected temporal scalings of the front properties revAduring various regimes as discussed in §3.2.1 and §3.2.2, has been provided in Table 2. Comparing the front advancements in Eqs. (19) and (26), it is noted that in the presence of mechanical dispersion, the front stays ahead as compared to a front which will be observed when only diffusion is active, although its rate of advancement is diminished. Similarly, comparing the reaction rates in Eq. (22) with those in Eq. (28), we observe that dispersion results in a slower growth rate of \bar{R} at early times, although its magnitude is still higher as compared to the dispersion-free scenario - see figures 3 and 4. More interestingly, comparing the reaction rates in Eq. (23) and Eq. (29), it is noted that dispersion may lead to a decaying global reaction rate at large times provided it remains dominant over diffusion; such a decay in \bar{R} is not observed when dispersion is absent. We discuss more on this in relation to figure 3.

Table 2: Expected temporal scalings of the front properties and the product mass based on the analytical approximations discussed in §3.2.1 and §3.2.2.

Front Property	Dispersion - Dominated Reaction-Limited ($t \ll 1, r_f \ll \eta Pe$)	Dispersion - Dominated Mixing-Limited ($t \gg 1, r_f \ll \eta Pe$)	Diffusion - Dominated Reaction-Limited ($t \ll 1, r_f \gg \eta Pe$)	Diffusion - Dominated Mixing-Limited ($t \gg 1, r_f \gg \eta Pe$)
r_f	$t^{1/3}$	$t^{1/3}$	$t^{1/2}$	$t^{1/2}$
w_f	$t^{1/3}$	t^0	$t^{1/2}$	$t^{1/6}$
\bar{R}	$t^{2/3}$	$t^{-1/3}$	t^1	t^0
M_C	$t^{5/3}$	$t^{2/3}$	t^2	t^1

3.2.3. The transition times

3.2.3.1. Transition time for the front's rate of advancement (r_f). For $Pe \sim 1$, we deduce from inference (iii) (see §3.2) that the front transitions into the diffusion-dominated region when it

reaches $r_f \sim \eta Pe \sim O(\eta)$. On the other hand, for $Pe \gg 1$, although the front is still in the dispersion-dominated region when it reaches $r_f \sim O(\eta)$ ($< \eta Pe$), condition (16) is no longer satisfied. Therefore, we deduce that the similarity solution (17) as well as the associated front propagation rate ($\mathcal{A}_{\text{disp}} t^{1/3}$, Eq. (19)) cease to be valid when $r_f \sim O(\eta)$. This leads to a transition in the front's rate of advancement, which occurs when $r_f = \mathcal{A}_{\text{disp}} t^{1/3} = \eta$, and yields the following estimate for the first transition time ($t_{\text{tr}}^{\text{disp}}$):

$$t_{\text{tr}}^{\text{disp}} = \left(\frac{\eta}{\mathcal{A}_{\text{disp}}} \right)^3 = \frac{\eta^2}{9 [\bar{\Gamma}^{-1}(\frac{1}{3}, \frac{1}{2})]} \approx 1.16 \eta^2. \quad (30)$$

It is to be noted that $t_{\text{tr}}^{\text{disp}}$ is independent of Pe and so is $\mathcal{A}_{\text{disp}}$, which indicates that the front's movement prior to $t_{\text{tr}}^{\text{disp}}$ (or, when $r_f < \eta$) is expected to be independent of Pe .

3.2.3.2. Transition time for the front characteristics into the Diffusion-dominated region. For $Pe \gg 1$, the front will continue to be in the dispersion-dominated region even after $t = t_{\text{tr}}^{\text{disp}}$, because $\eta < r_f < \eta Pe$. In such scenarios, the transition of the front properties into the diffusion-dominated regime occurs at a later time, when $r_f \sim \eta Pe$. Numerical solutions (see figures 3 and 4) suggest that during this transition, the front advances approximately as $r_f = \mathcal{A}_{\text{diff}} t^{1/2}$, yielding the following estimate for this second transition time ($t_{\text{tr}}^{\text{diff}}$):

$$t_{\text{tr}}^{\text{diff}} = \frac{\eta^2 Pe^3}{4 [\bar{\Gamma}^{-1}(\frac{Pe}{2}, \frac{1}{2})]}. \quad (31)$$

When $Pe \sim O(1)$, the above expression gives $t_{\text{tr}}^{\text{diff}} \approx 1.1 \eta^2$, indicating that the two transitions occur simultaneously. On the other hand, for $Pe \gg 1$, $t_{\text{tr}}^{\text{diff}} \approx 0.5 \eta^2 Pe^2 \gg t_{\text{tr}}^{\text{disp}}$.

3.2.3.3. General discussion on the transition times. Figure 2 summarizes the key inferences from the two transition times derived in §3.2.3.1 and 3.2.3.2. We can observe that below the $t_{\text{tr}}^{\text{disp}}/\eta^2$ curve (the solid pink region), mechanical dispersion dominates the transport on account of $t < t_{\text{tr}}^{\text{disp}}$. Similarly, above the $t_{\text{tr}}^{\text{diff}}/\eta^2$ curve (the solid violet region), where $t > t_{\text{tr}}^{\text{diff}}$, diffusion dominates the transport process over mechanical dispersion. In the region between the two curves (the hatched pink region), where $t_{\text{tr}}^{\text{disp}} < t < t_{\text{tr}}^{\text{diff}}$, the front resides in a dispersion-dominated region because $r_f < \eta Pe$ continues to be true, but the analytical scaling expectations derived in §3.2.1 do not remain valid here. In fact, during this period, the front's movement is closely approximated by the relation $r_f \sim \mathcal{A}_{\text{diff}} t^{1/2}$ (see figures 3 and 4), although it is not possible to derive analytical scaling expectations for the remaining front properties (as done in §3.2.1 and 3.2.2) during this time interval. One can observe that the length of this time interval grows with Pe . For $Pe = 1$,

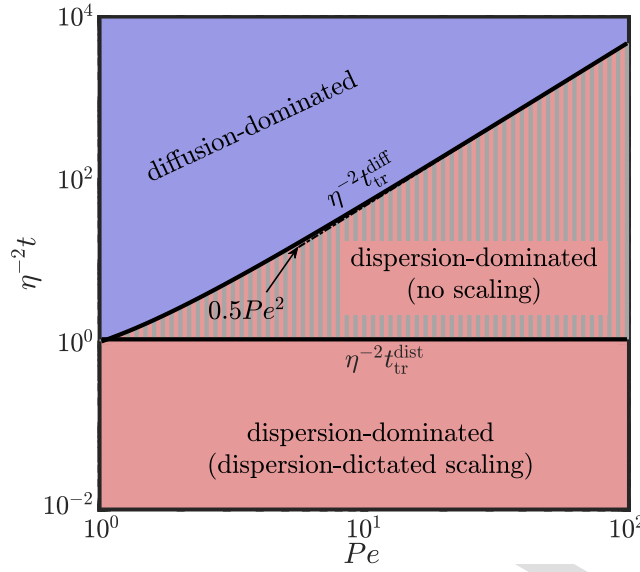


Figure 2: Plots of the normalized transition times t_{tr}^{disp}/η^2 and t_{tr}^{diff}/η^2 as functions of Pe .

the interval practically vanishes, thus indicating that for $Pe = 1$ the front's rate of advancement transitions at the same time as it moves into the diffusion-dominated region by crossing the threshold $r = \eta Pe$. Therefore, the other front properties are also expected to follow the diffusion-dominated scalings beyond this instant. Conversely, for $Pe \gg 1$, there are always two distinct transitions. The first one occurs at $t = t_{tr}^{disp}$, when the front's rate of advancement transitions from a $t^{1/3}$ -type behavior to a $t^{1/2}$ -type one. A second transition occurs later at $t = t_{tr}^{diff}$, when the front reaches a position $r = \eta Pe$ and the remaining front properties transition into the diffusion-dominated regime.

The quantification of the transition times discussed above also provides us with the conditions for the existence of several regimes outlined earlier. Specifically, the dispersion-dominated mixing-limited regime (§Appendix B.2) will be observed only if $t_{tr}^{disp} \gg 1$, while the diffusion-dominated reaction-limited regime (§Appendix B.3) materializes only when $t_{tr}^{diff} \ll 1$.

3.2.4. Results for $Pe = 1$

Figure 3 reports the variations in the front properties and the product mass with time, for $Pe = 1$ and for various choices of η . We have plotted the numerical solutions (solid lines) of the complete governing equation (Eq. (7)) along with the analytical temporal scalings (floating solid lines corresponding to the dispersion-dominated scalings from §3.2.1 and floating dashed-dot lines to the diffusion-dominated scalings from §3.2.2) for the various front properties. The star markers represent the time at which $r_f = \eta$ (representing $t \approx t_{tr}^{disp}$), which is also identical to the transition time from the dispersion-dominated into the diffusion-dominated regime, on account of $Pe = 1$.

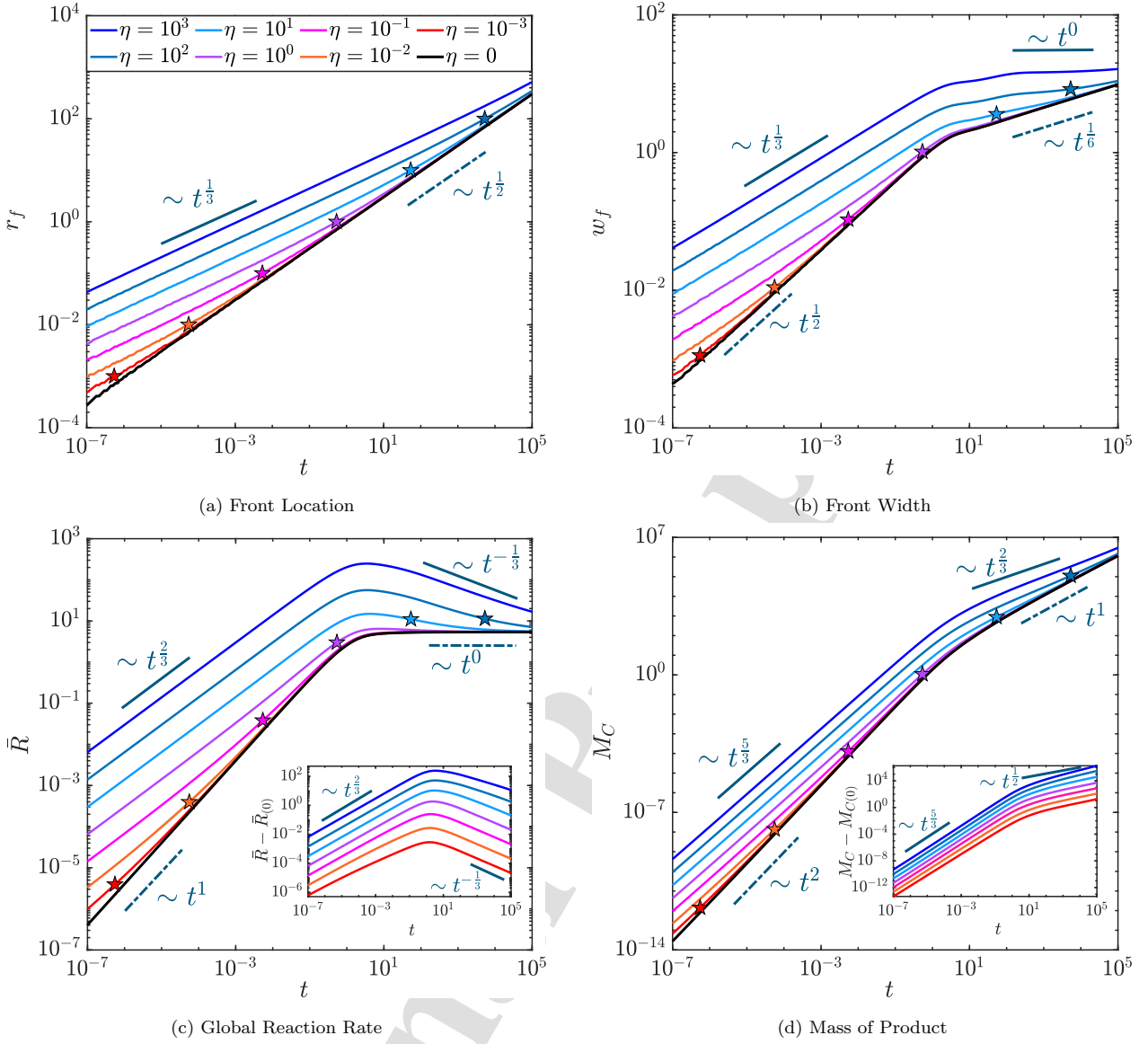


Figure 3: Time Evolution of the front properties and product mass for $Pe = 1$; the legend presented in panel (a) applies to all panels. The star markers demarcate the time at which $r_f = \eta$, which for $Pe = 1$ coincides with $r_f = \eta Pe$. The insets in panels (c) and (d) respectively show the excess global reaction rate and product mass, with respect to the dispersion-free scenario which is represented by the subscript '(0)' (e.g., $\bar{R}_{(0)}$).

The numerical results for the front location as well as the transition times agree well with the analytical estimates reported in Eqs. (19), (31) and (30).

We first note that the analytical scaling expectations as summarized in Table 2 show good agreement with the numerical solutions for all the front properties. For $\eta > 0$, the early time dispersion-dominated reaction-limited sub-regime ($t \ll 1$; $w_f \sim t^{1/3}$, $\bar{R} \sim t^{2/3}$, $M_C \sim t^{5/3}$, see

§3.2.1) may be clearly observed in all panels. At the same time, the diffusion-dominated reaction- and mixing-limited sub-regimes (see §3.2.2) are also evident when $\eta = 0$. The latter of these two sub-regimes is also observed at large times for the dispersive fronts, when $\eta \leq 10$. In particular, for $0 < \eta < 1$, one notes that the front transitions from the dispersion-dominated reaction-limited sub-regime into the diffusion-dominated reaction-limited sub-regime ($t \ll 1$; $w_f \sim t^{1/2}$, $\bar{R} \sim t^1$, $M_C \sim t^2$) at $t \approx t_{tr}^{disp} \approx t_{tr}^{diff}$, which occurs early ($t \ll 1$), also in agreement with the discussion in §3.2.3.3. Conversely, for $\eta \geq 10$, mechanical dispersion is strong enough to induce the dispersion-dominated mixing-limited sub-regime ($w_f \sim t^0$, $\bar{R} \sim t^{-1/3}$, $M_C \sim t^{2/3}$, see §3.2.1) for $t > 1$, as evident from panels (b) and (c). In such cases, the front directly approaches the diffusion-dominated mixing-limited sub-regime ($w_f \sim t^0$, $\bar{R} \sim t^{-1/3}$, $M_C \sim t^{2/3}$) at sufficiently large times, when by $t \approx t_{tr}^{disp} \approx t_{tr}^{diff} \gg O(1)$.

The inset in panel (c) reveals that hydrodynamic dispersion results in an enhanced global reaction rate at all times, as compared to the dispersion-free scenario ($\bar{R}_{(0)}$ for $\eta = 0$). Even at larger times, when molecular diffusion becomes the dominant Fickian mechanism driving mixing, mechanical dispersion still causes \bar{R} to be larger than $\bar{R}_{(0)}$, although now $\Delta\bar{R}(t) = \bar{R}(t) - \bar{R}_{(0)}(t)$ diminishes with time (at a rate $t^{-1/2}$). These features are also reflected in the excess product mass (ΔM_C), as shown in the inset of panel (d). Since $\Delta M_C = \int_0^t d\tau \Delta\bar{R}(\tau)$, ΔM_C should grow as $t^{1/2}$ at large times, as is indeed observed in the inset. As a result, although dispersion becomes subdominant at large times, it actually leads to an ever-increasing product mass as compared to the dispersion-free scenario, which underlines the profound impact of hydrodynamic dispersion on reactive transport in porous media.

The enhancement caused by the mechanical dispersion at early times also helps explain the the decaying (at $t^{-1/3}$) global reaction rate in the novel dispersion-dominated mixing-limited sub-regime. For sufficiently large η , the reactants are quickly consumed during the early time ($t < 1$) reaction-limited sub-regime, thus depleting the reactant concentration close to the front, which manifests in the decrement of \bar{R} at larger times ($t > 1$). This non-monotonic variation in the global reaction rate should also result in \bar{R} going through a maximum at $t \sim O(1)$, as is indeed observed in panel (c).

3.2.5. Results for $Pe = 100 \gg 1$

Figure 4 demonstrates the results for $Pe = 100$ (representing the limit $Pe \gg 1$), wherein the panel-wise description remains identical to fig. 3. The circular markers denote the time at which

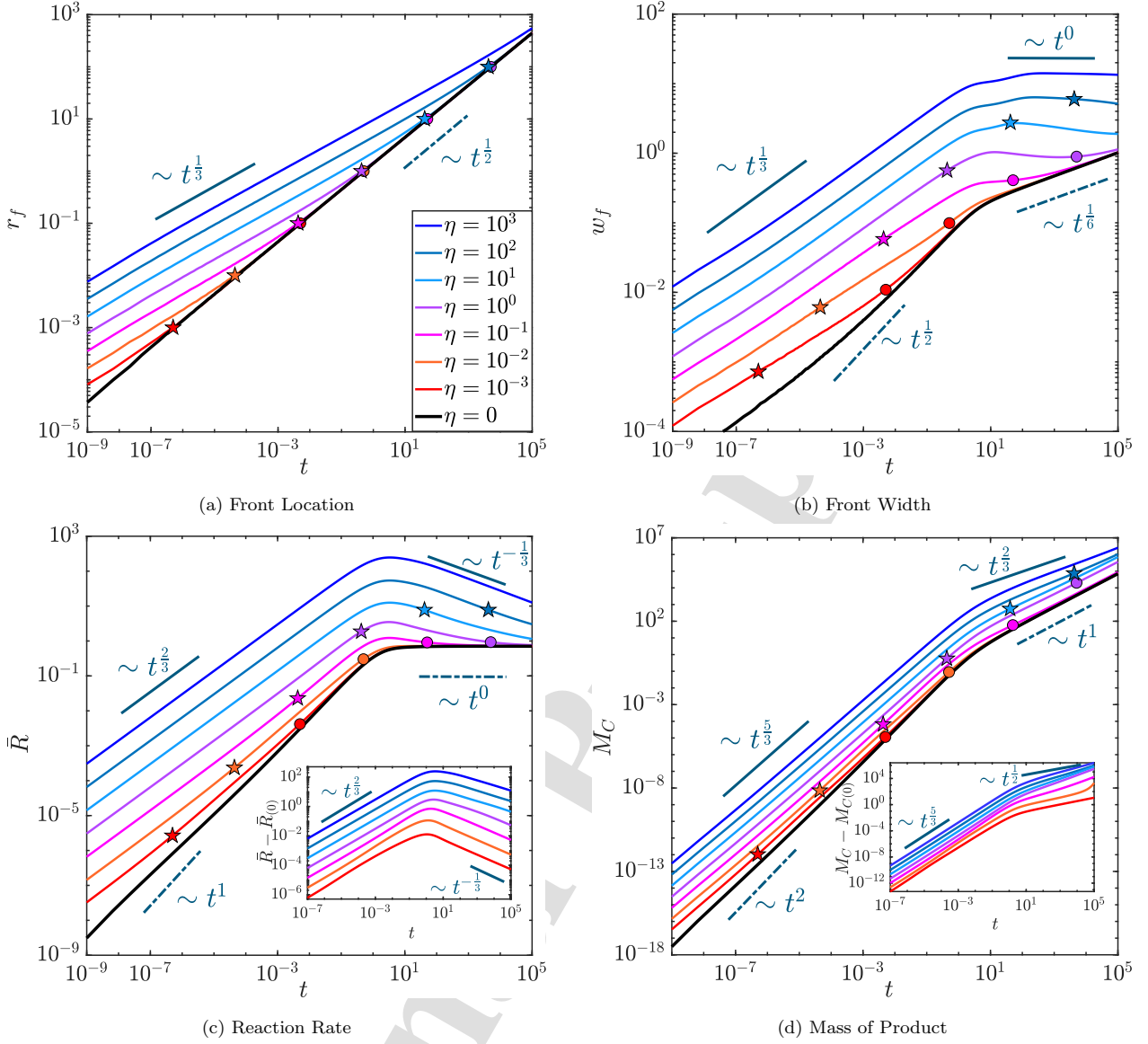


Figure 4: Time Evolution of the front properties and product mass for $Pe = 100$ and various choices of $\eta = 0, 10^{-3} - 10^3$. The star markers demarcate the instant when $r_f = \eta$ and the circular markers indicate the instant when $r_f = \eta Pe$. All other entities are the same as in Figure 3.

$r_f = \eta Pe$ (representing $t \approx t_{tr}^{diff}$). Recall from §3.2.3.1, that the condition (16) will now be satisfied for $t < t_{tr}^{disp}$ (the star markers), i.e., so long as $r_f \leq \eta$. We further note that the analytical scaling expectations as summarized in Table 2 have been included in all the panels and they show good agreement with the numerical results.

Qualitatively the variations shown in this figure are similar to those in Figure 3, with some subtle differences. In contrast to $Pe = 1$, the transition times t_{tr}^{disp} (star markers representing the

instant when $r_f \sim \eta$) and t_{tr}^{diff} are now separated by a significant time interval for $Pe = 100$; this is in agreement with Eqs. (30) and (31) and the discussion in §3.2.3.3. As a consequence, the transition of the front properties from the dispersion-dominated regime into the diffusion-dominated regime occurs much later than the transition in the front's location from a $t^{1/3}$ -type scaling into a $t^{1/2}$ -type behavior, as evident from panels (b) - (d). Because of a relatively larger value of Pe , molecular diffusion is relatively weak here and hence the front does not go through the diffusion-dominated reaction-limited sub-regime, even for η as small as 10^{-2} . In fact, for $\eta \geq 10^{-2}$, the front transitions from the dispersion-dominated regime directly into the diffusion-dominated mixing-limited sub-regime at large times.

The early time dispersion-dominated reaction-limited sub-regime ($t \ll 1$; $w_f \sim t^{1/3}$, $\bar{R} \sim t^{2/3}$, $M_C \sim t^{5/3}$) is present for all $\eta > 0$. The diffusion-dominated reaction-limited sub-regime only materializes for $\eta = 10^{-3}$ at $t_{tr}^{diff} < t < 1$ (for $\eta = 10^{-3}$, $t_{tr}^{diff} < 1$) and is made possible by the very weak mechanical dispersion. For all other values of η , t_{tr}^{diff} is larger than 1, which prevents this sub-regime from being realized. On the other hand, for $\eta = 10^2$ and 10^3 , $t_{tr}^{disp} > 1$ and hence the dispersion-dominated mixing-limited sub-regime ($w_f \sim t^0$, $\bar{R} \sim t^{-1/3}$, $M_C \sim t^{2/3}$) commences when $t \sim O(1)$. For $10^{-2} \leq \eta \leq 10$, although $t_{tr}^{disp} \sim O(10^{-1}) - O(1)$, there still is a relatively brief window reminiscent of this mixing-limited sub-regime, during which the global reaction rate decays (panel (c)) and the front width stays nearly constant (panel (b)). It may also be observed that at sufficiently large times (depending on the choice of η), all front properties eventually asymptote towards the $\eta = 0$ curve (dispersion-free), although for $\eta \geq 10^2$ this occurs beyond the time interval shown in the present figure. The insets in panels (c) and (d) reveal the same behavior as discussed in connection to Figure 3: hydrodynamic dispersion leads to an enhanced global reaction rate as compared to the purely diffusive scenario at all times, which in turn results in an ever increasing excess product mass when $\eta > 0$.

Intriguingly, comparing Figures 3 and 4, we observe that in the presence of mechanical dispersion, the front properties essentially become independent of Pe prior to t_{tr}^{disp} , which is in contrast to the dispersion-free scenario ($\eta = 0$) for which the front properties are generally dependent on Pe . This may be attributed to the fact that for $t < t_{tr}^{disp}$, Eq. (14) simplifies to $\partial_t \theta = \eta r^{-1} \partial_r^2 \theta$, which is independent of Pe and hence it is expected that the front properties emanating from this equation would also be independent of Pe . Conversely, when $\eta = 0$ or for $t > t_{tr}^{disp}$, the governing equations can not be made independent of Pe and hence the front properties also exhibit Péclet

number dependent variations.

3.2.6. Phase diagrams of the front behavior

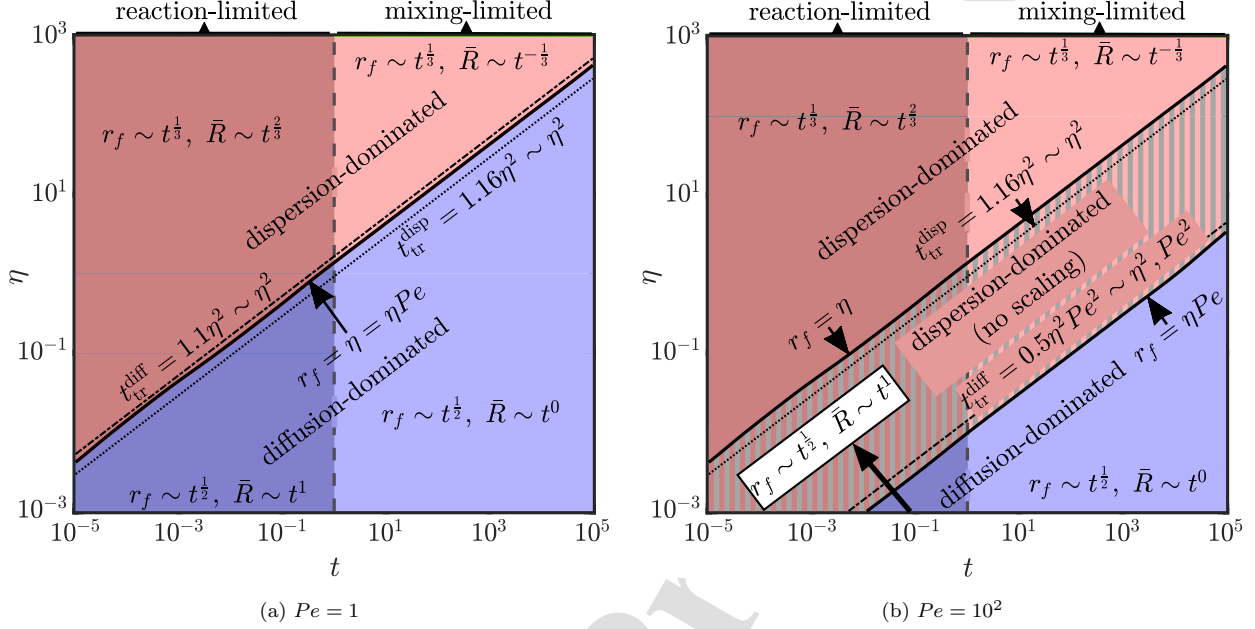


Figure 5: Phase diagram summarizing the various regimes of the reactive transport process in the (η, t) plane along with the expected scalings as summarized in Table 2. The vertical dashed line demarcates the instant $t = 1$. The solid black lines represent the numerically evaluated time at which the front passes through $r_f = \eta$ and ηPe ; they coincide for $Pe = 1$. The dotted and dashed-dot black lines show the transition times t_{tr}^{disp} and t_{tr}^{diff} respectively as functions of η , as estimated based on Eqs. (30) and (31). Panel (a) is for $Pe = 1$ and panel (b) for $Pe = 100$.

Figure 5 summarizes the various regimes and sub-regimes of a radially advected reaction front in the presence of dispersion on the (η, t) plane. All the associated temporal scalings for the front location and the global reaction rate have been indicated within the figure (also summarized in Table 2). Examining both the panels, it appears that t_{tr}^{disp} and t_{tr}^{diff} respectively approximate the actual (i.e., numerically obtained) transitions at $r_f = \eta$ and $r_f = \eta Pe$ reasonably well.

We first note that the two regime diagrams qualitatively look very similar, and as such, one can clearly identify four distinct areas. These correspond to the four sub-regimes: (i) the dispersion-dominated reaction-limited sub-regime (dark pink, solid, §Appendix B.1); (ii) the diffusion-dominated reaction-limited sub-regime (dark violet §Appendix B.3) for sufficiently weak dispersion and advection; (iii) the dispersion-dominated mixing-limited sub-regime (light pink, solid, §Appendix B.2) for strong mechanical dispersion; (iv) the diffusion-dominated mixing-limited sub-regime (light violet, solid, §Appendix B.4). In addition, panel (b) contains two more areas, i.e., (v) the hatched

dark pink and (vi) the hatched light pink areas, which exist because for $Pe = 100$, $t_{tr}^{disp} < t_{tr}^{diff}$ and hence the front goes through two distinct transitions as outlined in §3.2.3. Noting that these two areas are sandwiched between the t_{tr}^{disp} and t_{tr}^{diff} curves, one may infer that they both imply dispersion-dominated regime but without any analytical scaling expectations, since $t_{tr}^{disp} < t < t_{tr}^{diff}$ in these two areas – also see §3.2.3.3 for details. The area (v) (dark pink, hatched) is part of the dispersion-dominated reaction-limited sub-regime for the time interval $t_{tr}^{disp} < t < 1$ and the area (vi) (light pink, hatched) is part of the dispersion-dominated mixing-limited sub-regime for the time interval $1 < t < t_{tr}^{diff}$. Consequently, when $Pe = 1$, i.e. when $r_f = \eta$ and $r_f = \eta Pe$ become identical, the hatched areas ((v) and (vi)) vanish, as observed in panel (a), which implies a simultaneous transition in the front's advancement and in all other front characteristics at $r_f = \eta = \eta Pe$. We have verified that the overall nature of the phase diagram as shown in Figure 5 remains unaltered for other values of Pe ; a larger Pe would result in widening of the hatched area illustrated in panel (b), and push the diffusion-dominated areas (violet) further south-east, whilst the dispersion-dominated areas above the $r_f = \eta$ curve (solid pink) are only affected to a negligible extent. Above the $t = t_{tr}^{disp}$ curve, the front behavior is dominated by mechanical dispersion, while below the $t = t_{tr}^{diff}$ curve, diffusion controls the front behavior.

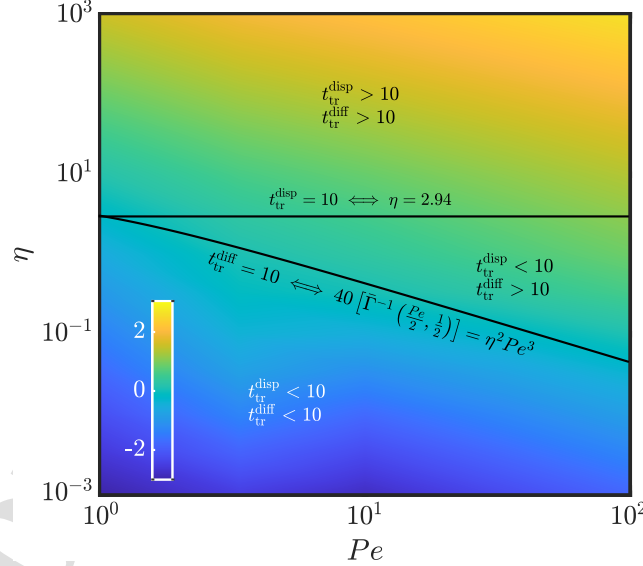


Figure 6: Surface plot of $\log_{10}(\Delta M_C/M_{C(0)})$ at time $t = t_* = 10$ in the (η, Pe) plane, where $\Delta M_C = M_C - M_{C(0)}$. The black solid curves represent $t_{tr}^{disp} = 10$ and $t_{tr}^{diff} = 10$ as labeled.

It is noteworthy that in the presence of mechanical dispersion, the global reaction rate and the product mass never fall below those obtained in the dispersion-free scenario. Hence, hydrodynamic

dispersion enhances the global reaction rate at early times, whilst still not adversely affecting it at large times, although for $t \gg 1$, the front properties asymptotically approach their dispersion-free counterparts. Despite this, the accumulated product mass is still expected to have a signature of the dispersion-driven enhanced reaction rates at earlier times. We have quantified this in terms of the excess product mass ($\Delta M_C = M_C - M_{C(0)}$), in the insets of Figures 3d and 4d. The large time signature of dispersion on the product mass (evaluated at $t = t_* = 10$) is further investigated in Figure 6. Below the $t_{tr}^{diff} = 10$ curve, where both $t_{tr}^{disp} < t_* = 10$ and $t_{tr}^{diff} < t_* = 10$, the enhancement in the product mass due to dispersion is very limited, as the front has already transitioned into the diffusion-dominated regime by the time $t = t_* = 10$ is reached. In between the two black curves, where $t_{tr}^{disp} < 10$, but $t_{tr}^{diff} > 10$, the front resides in the dispersion-dominated regime at $t = t_* = 10$ (as $r_f < \eta Pe$), and therefore, we observe a moderate enhancement in the product mass. The maximum augmentation in M_C is however observed above the curve $t_{tr}^{disp} = t_* = 10$, where both $t_{tr}^{disp} > 10$, and $t_{tr}^{diff} > 10$ and hence the front at time $t = t_* = 10$ is still completely within the dispersion-dominated regime, being dictated by the scalings established in §3.2.1. Generally, larger η and Pe both facilitate larger ΔM_C by delaying the onset of the diffusion-dominated regime.

3.3. Illustrative practical examples related to the subsurface porous media

The reactive front dynamics discussed in the preceding sections are in terms of dimensionless numbers, providing general insights into the reactive transport processes in a porous media. It is thus important, from an application perspective, to relate the results of the present analysis to reactions that are often encountered in the subsurface porous media for various purposes. To this end, in table 3, we list the typical values of the key dimensionless parameters and characteristic scales for some common scenarios relevant to subsurface applications.

Figure 7 revisits the phase diagrams in figures 2 and 5 in dimensional terms, translated to the (Q_0, t') plane and the (t', t_R) plane respectively, where t' is the time after injection and t_R is the reaction time scale. The color coding of the various regimes remains identical to those used earlier. The flow rates considered in the two panels correspond to the typical flow rates encountered in subsurface injection scenarios such as environmental restoration (Narr, 1996; Saripalli et al., 2000; Zhang, 2003; Phenrat and Lowry, 2019). Similarly, the range of characteristic time scales in table 3 correspond to the typical reaction times encountered in various subsurface scenarios (Sundstrom et al., 1986; Patil and Sharma, 2011; Rossi et al., 2015; Haynes et al., 2016).

First and foremost, we observe from figure 7 (both panels) that for typical subsurface flow

Table 3: Range of values for the characteristic scales (t_c & r_c) and the non-dimensional parameters (Pe and η). Three distinct values of the longitudinal dispersion length (ℓ_L) have been illustrated along with the corresponding values of η .

Parameter	Range			
Péclet number Pe	10^0 – 10^4			
Characteristic Time Scale t_c (s)	10^2 – 10^{10}			
Characteristic Length Scale r_c (m)	10^{-2} – 10^3			
Long. Dispersion length ℓ_L (m)	0	10^{-3}	10^0	10^3
Dimensionless long. dispersion length η	0	10^{-6} – 10^{-1}	10^{-3} – 10^2	10^0 – 10^5

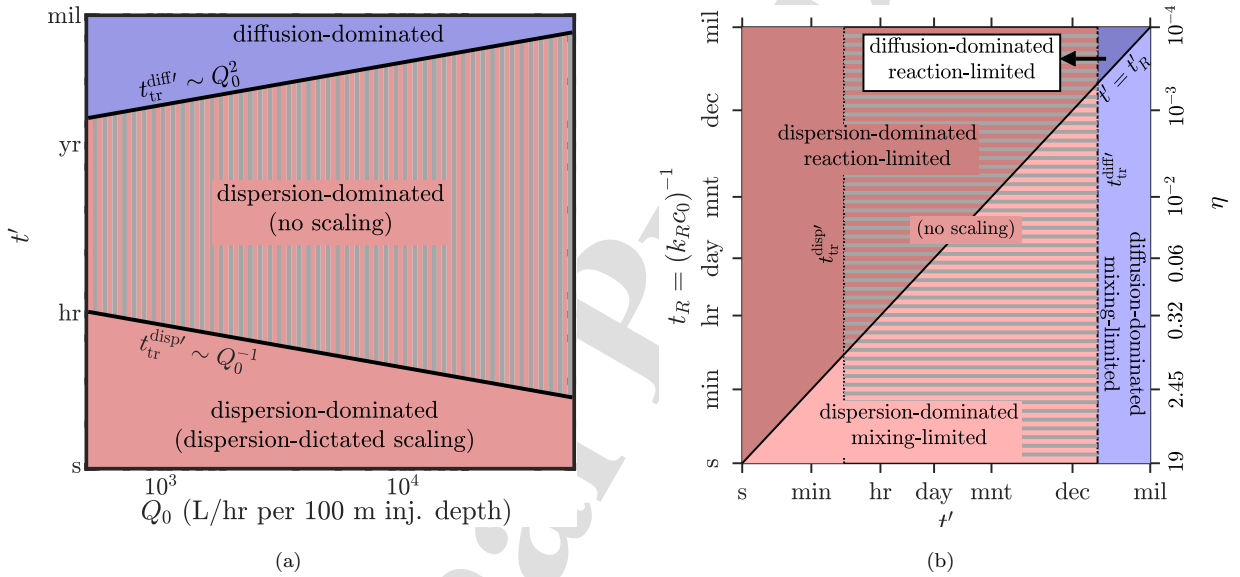


Figure 7: (a) Plots of the dimensional transition times (with units) t_{tr}^{disp} and t_{tr}^{diff} as functions of Q_0 for $\ell_L = 10$ cm and $\phi_0 = 0.5$, with the three regimes delimited by these transition times. (b) Dimensional phase diagram for a porous domain having a porosity ϕ_0 of 0.5, for $Q_0 = 5000$ L/hr per 100 m of injection depth (i.e., $Q_0 = 1.39 \times 10^{-5}$ m³/m.s) ($Pe = 2.78 \times 10^3$), depicting the various regimes of the reactive transport process in the (t', t_R) plane where t' is the dimensional time and t_R is the reaction time scale ($= (k_R c_0)^{-1}$). The solid black diagonal line represents $t' = t'_R$. The dotted and dashed-dotted vertical lines respectively demarcate the transition times $t_{tr}^{disp} = 1.16 \ell_L^2 / Q_0$ and $t_{tr}^{diff} = \ell_L^2 Q_0^2 / (4 D_M^3 \Gamma^{-1} [Q_0 / (2 D_M), 1/2])$. The hatched pink region corresponds to the dispersion-dominated behavior without any analytical scaling expectations. The diffusion coefficient and the dispersion length have been fixed to $D_M = 10^{-8}$ m²/s and $\ell_L = 10$ cm. The right vertical axis indicates the variations in η ; the ticks 'mnt' and 'mil' stand for a month and a thousand years respectively.

rates ($Q_0 \sim 10^3 - 10^5$ L/hr. per 100 m depth), the reaction front will remain well within the

dispersion-dominated region for any realistic time-frame, thus underlining the impact of mechanical dispersion on the transport processes. The transition of the front into the diffusion-dominated region depends on the flow rate and may take anywhere from a few years to a several decades. We further observe that the transition times ($t_{tr}^{disp'}$ and $t_{tr}^{diff'}$) are independent of the reaction time (as they are represented by vertical lines in panel (b)) and depend only on the flow rate and the dispersion length. A larger flow rate does not qualitatively alter the phase diagram in panel (b), rather it only widens the hatched region between the two transition times because $t_{tr}^{disp'}$ decays as Q_0^{-1} and $t_{tr}^{diff'}$ increases as Q_0^2 (see panel 7a). Thus, a larger flow rate generally delays the onset of the diffusion-dominated regime, thereby enhancing the influence of mechanical dispersion on the reaction, whilst also resulting in an earlier transition in the front's rate of advancement (r_f). Similarly, a larger dispersion length will also not alter the qualitative nature of the phase diagram and will only delay the two transitions (with all other entities remaining unchanged), since both of them increase as ℓ_L^2 . The diagonal $t' = t_R$ line in panel (b) separates the reaction-limited and the mixing-limited regimes. Therefore, faster reactions (smaller t_R) would cross this curve at an earlier time, before even crossing the $t' = t_{tr}^{diff'}$ line. Conversely, sufficiently slow reactions (large t_R) may transition into the diffusion-dominated regime before crossing the $t' = t_R$ curve.

It is observed that for a given flow rate and dispersion length, faster reactions result in larger η values and thus mechanical dispersion will have a greater influence on their kinetics. In fact, faster reactions generally go through the dispersion-dominated reaction-limited sub-regime when $t' < t_R$, followed by the dispersion-dominated mixing-limited sub-regime at $t_R < t' < t_{tr}^{diff'}$, and they finally enter the diffusion-dominated mixing-limited sub-regime at $t_{tr}^{diff'} < t'$. Conversely, the impact of hydrodynamic dispersion is relatively weaker on slow reactions as they tend to result in lower values of η ; sufficiently slow reactions would be in the dispersion-dominated reaction-limited sub-regime at $t' < t_{tr}^{diff'}$, and then move on to the diffusion-dominated reaction-limited sub-regime when $t_{tr}^{diff'} < t' < t_R$, before transitioning into the diffusion-dominated mixing-limited sub-regime when $t' > t_R$. Based on the above discussion, it may therefore be concluded that faster reactions and higher flow rates will maximize the influence of dispersion on reactive transport processes. While specific parameter sets will provide specific estimations, broadly speaking, a larger flow rate and/or a larger dispersion length will facilitate greater advancement of the front along with a larger reaction rate and a larger product mass.

Finally, recalling that we assume axisymmetry of the flow (which requires that the pore scale

flow is at worse weakly-nonlinear and hence $Re \leq O(1)$, see section 2.1), we note that the pore-scale Reynolds number may be defined as $Re = av'/\nu$, where $v' = Q_0/(\phi_0 r')$, a being the characteristic length scale of the pores ($a \sim \sqrt{k}$, where k is the permeability) and ν is the kinematic viscosity of water. Taking $a \sim 3 \times 10^{-6}$ m (corresponding to $k \sim 10^{-11}$ m²), $Q_0 \sim 1.4 \times 10^{-5}$ m³/m.s and $\phi_0 = 0.5$, the above condition is satisfied when $r' > Q_0 a / \phi_0 \nu \simeq 10^{-4}$ m, which indicates that our axisymmetric solution can be considered to be valid in the entire porous medium outside of the injection borehole.

4. Conclusion

In this article, reactive transport in a radially moving A+B→C bimolecular reaction front has been studied in the presence of significant hydrodynamic dispersion. The species A was continually injected into an infinite porous medium of uniform permeability, which initially only contained the species B. The advection-dispersion-reaction equation was solved to infer the spatio-temporal evolution of the reactants' and the product's concentrations. Both numerical and approximate analytical solutions were derived, the latter being applicable to various temporal regimes; the numerical and analytical solutions agreed well with each other.

There are several novel points to be noted from our analysis. First, it is established that at early times ($t \ll 1$), mechanical dispersion is dominant over molecular diffusion and the front thus advances as $r_f \sim t^{1/3}$, which is qualitatively different from a $t^{1/2}$ -type progress observed when diffusion is the only Fickian mixing mechanism. This results in a dispersion-dominated regime and leads to enhanced global reaction rates (and thus an enhanced product mass) at the early reaction-limited times. The $r_f \sim t^{1/3}$ -type variation in the front's movement ceases to be valid when the front reaches the location $r_f \sim \eta$; this leads to a transition (at $t = t_{tr}^{disp}$) in the behavior of the front's position from a $t^{1/3}$ to a $t^{1/2}$ -type scaling in time. When $Pe \sim O(1)$, the front completely transitions into the diffusion-dominated regime at this juncture, because the condition $r_f \sim \eta Pe$ is also satisfied. However, when $Pe \gg 1$, the front still remains in the dispersion-dominated region after this first transition, and a second transition occurs only when the front crosses the location $r_f \sim \eta Pe$, at a time $t = t_{tr}^{diff}$ at which the diffusion-dominated regime sets in.

Within the dispersion-dominated regime, the front exhibits reaction-limited behavior at early times ($t \ll 1$), and may exhibit mixing-limited behavior at moderately large times ($t \gg 1$), provided that mechanical dispersion (η) is sufficiently strong. This second sub-regime is characterized by a

decaying global reaction rate and a nearly constant front width. Furthermore, the global reaction rate (\bar{R}) also goes through a maximum at $t \sim O(1)$, when the dispersion-dominated mixing-limited sub-regime sets in. At sufficiently large times, regardless of the strength of dispersion, its impact will eventually become subdominant and the front will transition into a diffusion-dominated regime. However, when dispersion is weak ($\eta < 1$), the front will leave the dispersion-dominated region sufficiently early so that a diffusion-dominated reaction-limited sub-regime may come into existence before $t = 1$, followed by the diffusion-dominated mixing-limited sub-regime.

The reaction front behavior is expected to remain dominated by dispersion for any realistic time frame of field scale experiments, because the time of transition of the front into the diffusion-dominated behavior may vary from several years to several decades, depending on the flow rate and the dispersion length. In particular, mechanical dispersion is observed to influence faster reactions to a greater extent, with all other parameters remaining unchanged. Generally, the presence of hydrodynamic dispersion leads to enhanced reaction rates and product mass as compared to a dispersion-free scenario; this is true at all times, although at large times ($t > 1$) the differences between the two decay with time.

The above findings may provide fundamental insights towards characterizing reactive front dynamics and help formulate transport models for a diverse set of applications related to subsurface porous media such as contaminant remediation, aquifer recharge, geothermal systems, to underline a few. Future studies should investigate some key elements that have not been considered here. This includes: the impact of macroscopic permeability heterogeneities, which are expected to further enhance mixing rates due to stretching of the front, the effect of non-Fickian dispersion, which would affect scaling laws, and the case of partially penetrating wells, which would lead to imperfect radial flows. While we have investigated here a simplified bimolecular reaction, it would also be useful to confirm the predicted dynamics for realistic geochemical processes simulated with a multi-component reactive transport model.

Acknowledgments

PK is grateful to IIT Gandhinagar for Early Career Fellowship (ref: MIS/IITGN/ME/UG/2021 22/043). UG is grateful to SERB, Government of India, for providing financial support for this work through the Ramanujan Fellowship (ref: SB/S2/RJN-180/2017).

Appendix A. Numerical solution methodology

Eq. (7) is discretized as per the time-implicit finite difference method:

$$(\eta Pe v_{r(j)} + 1) T_1 + \left(\frac{(\eta Pe v_{r(j)} + 1)}{r_{(j)}} + \eta \frac{dv_r}{dr} \Big|_{(j)} \right) T_2 - Pe v_{r(j)} T_3 - \left(\frac{Pe}{t - t^{\text{prev}}} + S_{P,i(j)} \right) c_{i(j)} = - \frac{Pe c_{i(j)}^{\text{prev}}}{t - t^{\text{prev}}} + S_{C,i(j)}, \quad (\text{A.1})$$

$$T_1 = \frac{2(r_j - r_{j-1})c_{i(j+1)} - 2(r_{j+1} - r_{j-1})c_{i(j)} + 2(r_{j+1} - r_j)c_{i(j-1)}}{(r_{j+1} - r_j)(r_{j+1} - r_{j-1})(r_j - r_{j-1})} \quad (\text{A.2})$$

$$T_2 = \frac{(r_j - r_{j-1})c_{i(j+1)} + (r_{j+1} + r_{j-1} - 2r_j)c_{i(j)} - (r_{j+1} - r_j)c_{i(j-1)}}{2(r_{j+1} - r_j)(r_j - r_{j-1})} \quad (\text{A.3})$$

$$T_3 = \frac{(r_{j-1} - r_{j-2})(2r_j - r_{j-1} - r_{j-2})c_{i(j)} - (r_j - r_{j-2})^2 c_{i(j-1)} + (r_j - r_{j-1})^2 c_{i(j-2)}}{(r_{j-1} - r_{j-2})(r_j - r_{j-1})(r_j - r_{j-2})} \quad (\text{A.4})$$

The numerical solution is obtained by time-marching, wherein Eq. (A.1) is solved at each time step for each of the three species, A, B and C, with $v_{r(j)} = 1/r_j$. The term $c_{i(j)}$ represents the i -th species concentration at the j -th grid point, and the superscript ‘prev’ denotes that the value is for the previous time step. At each time step, iterations are carried out till the error $(1/n) \sum_{i=1}^{i=3} \sum_{j=1}^{j=n} (c_{i(j)} - c_{i(j)}^{\text{last}})^2$ (n is the number of nodes on the discretized x -axis) falls below the tolerance (here, taken as 10^{-5}) with $c_{i(j)}^{\text{last}}$ being the solution of the last iteration. These iterations are carried out to resolve the non-linear reaction terms, wherein these terms are expanded in a Taylor series around the solutions from the previous iteration (or, for the first iteration, the initial guess). This procedure is commonly known as the source-term linearization technique (Patankar, 2018), and is implemented as follows: $R_{i(j)} \approx S_{C,i(j)} + S_{P,i(j)} c_{i(j)}$, where $S_{C,i(j)} = R_{i(j)}^{\text{last}} - \delta R_i / \delta c_i|_{(j)}^{\text{last}} c_{i(j)}^{\text{last}}$, $S_{P,i(j)} = \delta R_i / \delta c_i|_{(j)}^{\text{last}}$ and the superscript ‘last’ indicates that the given quantity is evaluated using the solutions from the previous iteration. Using (7b), $S_{C,i(j)}$ and $S_{P,i(j)}$ get evaluated as: for species A, $S_{P,A(j)} = -c_{B(j)}^{\text{last}}$, $S_{C,A(j)} = 0$; for B, $S_{P,B(j)} = -c_{A(j)}^{\text{last}}$, $S_{C,B(j)} = 0$, and for C, $S_{P,C(j)} = 0$, $S_{C,C(j)} = c_{A(j)}^{\text{last}} c_{B(j)}^{\text{last}}$. Lastly, knowing that the system evolves slowly at long times and the gradients are smoother at larger r , the t and r grids are discretized in a non-uniform fashion, being finer near $t/r = 0$ and relatively coarser for $t/r \gg 1$.

Appendix B. Temporal scalings for the front properties and the product mass

The solution for θ and the front location, as expressed in Eqs. (17), (19), (25) and (26) for the dispersion and diffusion-dominated regimes may be unified in the following manner:

$$\theta = -1 + 2\bar{\Gamma}(\gamma_{\text{dom}}, \xi_{\text{dom}}), \quad (\text{B.1a})$$

$$r_f = \mathcal{A}_{\text{dom}} t^{\gamma_{\text{dom}}}, \quad (\text{B.1b})$$

where ‘dom’ \equiv ‘disp’ signifies the dispersion-dominated regime, while ‘dom’ \equiv ‘diff’ indicates that diffusion is dominant over mechanical dispersion. As such, we note that, $\gamma_{\text{disp}} = 1/3$, $\xi_{\text{disp}} = r^3/(9\eta t)$, $\gamma_{\text{diff}} = 1/2$, and $\xi_{\text{diff}} = (Pe r^2)/(4t)$. Furthermore, with the expressions for θ and r_f as presented in Eq. (B.1), a Taylor series expansion for θ around the front,

$$\theta = \theta_f^0 + (r - r_f) \left[\frac{\partial \theta}{\partial r} \right]_f + O((r - r_f)^2) \approx -\mathcal{K}_{\text{dom}} t^{-\gamma_{\text{dom}}} (r - r_f), \quad (\text{B.2})$$

with $\mathcal{K}_{\text{disp}} = 6 \left(9^{\frac{1}{3}} \eta^{\frac{1}{3}} \exp(\mathcal{A}_{\text{disp}}^3/(9\eta)) \right)^{-1}$ and $\mathcal{K}_{\text{diff}} = 2\sqrt{Pe} \left(\exp((Pe \mathcal{A}_{\text{diff}}^2)/4) \right)^{-1}$, simplifies the subsequent analysis. In an effort to obtain further insights into the reaction front’s behavior, recall from Eq. (20) that we approximate c_A as:

$$c_A = t^{-\frac{\beta}{2}} G(z), \quad z = \frac{r - r_f}{t^\alpha}, \quad (\text{B.3})$$

and further utilizing Eq. (B.2), the expression for c_B (which is $c_A - \theta$) becomes:

$$c_B = t^{-\beta/2} (G(z) + \mathcal{K}_{\text{dom}} z). \quad (\text{B.4})$$

Proceeding with these expressions, Eq. (8a) may be simplified for various temporal regimes and dispersion strengths to yield the respective ODEs for $G(z)$ in the vicinity of the reaction front. The region far behind the front corresponds to $z \rightarrow -\infty$, which is also the left boundary for these ODEs. In this region, since $c_B = 0$, one must have $c_A = \theta$, which leads to (upon equating Eqs. (B.3) and (B.2)) $G(z) \sim -t^{\alpha+\beta/2-\gamma_{\text{dom}}} \mathcal{K}_{\text{dom}} z$, as $z \rightarrow \infty$. Because G is a function of z only as per Eq. (20), it follows that $\alpha + \beta/2 - \gamma_{\text{dom}} = 0$ and $G \sim -\mathcal{K}_{\text{dom}} z \propto -z$ as $z \rightarrow -\infty$. The arguments presented above are analogous to those utilized by Gálfi and Rácz (1988) in their study of planar reaction fronts, and adopted later by various others (Braun and De Wit, 2020; Comolli et al., 2019).

We now conduct the following algebraic manipulations on equation (8a):

1. Substitute c_A and c_B from Eqs. (B.3) and (B.4) respectively, into Eq. (8a). Note that while substituting c_A , the derivatives $\partial c_A / \partial t$, $\partial c_A / \partial r$ and $\partial^2 c_A / \partial r^2$ are evaluated as $-t^{-\frac{\beta}{2}-1} [\beta G/2 + \alpha z dG/dz]$, $t^{-\alpha-\beta/2} dG/dz$, and $t^{-2\alpha-\beta/2} d^2 G/dz^2$, respectively.
2. Substitute $r = r_f + z t^\alpha$ using equation (B.3) and $r_f = \mathcal{A}_{\text{dom}} t^{\gamma_{\text{dom}}}$, as per equation (B.1b).
3. Multiply either sides of the resulting equation by $t^{\alpha+\frac{\beta}{2}-\gamma_{\text{dom}}} (\mathcal{A}_{\text{dom}} t^{\gamma_{\text{dom}}} + z t^\alpha)$.

The above steps lead to the following governing equation for $G(z)$ in the vicinity of the front:

$$Pe (\mathcal{A}_{\text{dom}} t^{\gamma_{\text{dom}}} + z t^{\alpha}) \left[t^{2\alpha-2\gamma_{\text{dom}}} (G^2 + \mathcal{K}_{\text{dom}} z G) - t^{\alpha-1-\gamma_{\text{dom}}} \left(\frac{\beta}{2} G + \alpha z \frac{dG}{dz} \right) \right] = (\eta Pe + \mathcal{A}_{\text{dom}} t^{\gamma_{\text{dom}}} + z t^{\alpha}) t^{-\alpha-\gamma_{\text{dom}}} \frac{d^2 G}{dz^2} + (1 - Pe) t^{-\gamma_{\text{dom}}} \frac{dG}{dz}. \quad (\text{B.5})$$

Note that the $(\eta Pe + \mathcal{A}_{\text{dom}} t^{\gamma_{\text{dom}}} + z t^{\alpha})$ term simplifies to (ηPe) when dispersion dominates ('dom' \equiv 'disp') and to $(\mathcal{A}_{\text{dom}} t^{\gamma_{\text{dom}}} + z t^{\alpha})$ when diffusion dominates ('dom' \equiv 'diff').

On the other hand, substituting r_f from Eq. (B.1b) and the similarity expressions for c_A and c_B from Eqs. (B.3) and (B.4) respectively, with r expressed in terms of t and z as noted above, a general expression for \bar{R} based on Eq. (11) may be written as,

$$\bar{R}(t) = 2\pi \int_{-\infty}^{\infty} (G^2 + \mathcal{K}_{\text{dom}} z G) (\mathcal{A}_{\text{dom}} + z t^{\alpha-\gamma_{\text{dom}}}) t^{\alpha-\beta+\gamma_{\text{dom}}} dz = \mathbb{I}_{\mathbb{R}} t^{\alpha-\beta+\gamma_{\text{dom}}} \propto t^{\alpha-\beta+\gamma_{\text{dom}}}, \quad (\text{B.6})$$

where $\mathbb{I}_{\mathbb{R}} = 2\pi \int_{-\infty}^{\infty} (G^2 + \mathcal{K}_{\text{dom}} z G) (\mathcal{A}_{\text{dom}} + z t^{\alpha-\gamma_{\text{dom}}}) dz$. This is independent of time because at early times ($t \ll 1$), $\alpha = \gamma_{\text{dom}}$ and hence $t^{\alpha-\gamma_{\text{dom}}} = 1$, while at large times ($t \gg 1$), $\alpha < \gamma_{\text{dom}}$ and hence $t^{\alpha-\gamma_{\text{dom}}} \rightarrow 0$, in both the dispersion-dominated regime as well as the diffusion-dominated regimes (see table 2). Refer to Appendix C for a detailed derivation of the values of α and β during the various temporal regimes.

In order to obtain the temporal scaling for the front width w_f , we substitute, $r = r_f + z t^{\alpha}$ and $c_A = t^{-\frac{\beta}{2}} G(z)$ using Eq. (B.3), $r_f = \mathcal{A}_{\text{dom}} t^{\gamma_{\text{dom}}}$ using Eq. (B.1b) and $c_B = t^{-\frac{\beta}{2}} (G(z) - \mathcal{K}_{\text{dom}} z)$ using Eq. (B.4), into Eq. (10). Furthermore, $dr = t^{\alpha} dz$ for a fixed time, whereas the integration limits $r \rightarrow 0$ and $r \rightarrow \infty$ transforms to $z \rightarrow -\infty$ and $z \rightarrow \infty$ respectively. This yields:

$$w_f = \left[\frac{\int_{z \rightarrow -\infty}^{z \rightarrow \infty} 2\pi (\mathcal{A}_{\text{dom}} t^{\gamma_{\text{dom}}} + z t^{\alpha}) t^{-\beta} (G^2 - \mathcal{K}_{\text{dom}} z) (z t^{\alpha})^2 t^{\alpha} dz}{\int_{z \rightarrow -\infty}^{z \rightarrow \infty} 2\pi (\mathcal{A}_{\text{dom}} t^{\gamma_{\text{dom}}} + z t^{\alpha}) t^{-\beta} (G^2 - \mathcal{K}_{\text{dom}} z) t^{\alpha} dz} \right]^{\frac{1}{2}} = \mathbb{I}_{\mathbb{W}} t^{\alpha} \propto t^{\alpha} \quad (\text{B.7a})$$

$$\text{where, } \mathbb{I}_{\mathbb{W}} = \left[\frac{\int_{z \rightarrow -\infty}^{z \rightarrow \infty} (\mathcal{A}_{\text{dom}} + z t^{\alpha-\gamma_{\text{dom}}}) (G^2 - \mathcal{K}_{\text{dom}} z) z^2 dz}{\int_{z \rightarrow -\infty}^{z \rightarrow \infty} (\mathcal{A}_{\text{dom}} + z t^{\alpha-\gamma_{\text{dom}}}) (G^2 - \mathcal{K}_{\text{dom}} z) dz} \right]^{\frac{1}{2}}, \quad (\text{B.7b})$$

like $\mathbb{I}_{\mathbb{R}}$, is independent of time.

Appendix B.1. The early time dispersion-dominated reaction-limited sub-regime ($t \ll 1$ and $r_f \ll \eta Pe$)

For $t \ll 1$ and $r_f \ll \eta Pe$, we show in Appendix C.1 that $\alpha = 1/3$ (giving us $\beta = 0$) is required for Eq. (B.5) to remain physically consistent. As a consequence Eq. (B.5) simplifies to: $d_z^2 G + (\mathcal{A}_{\text{disp}} z + z^2)/(3\eta) d_z G = 0$, where d_z^2 represents second total derivative with respect to z . Using Eq. (B.6), one then obtains:

$$\bar{R}(t) = 2\pi \int_{-\infty}^{\infty} (G^2 + \mathcal{K}zG) (\mathcal{A}_{\text{disp}} + z) t^{\frac{2}{3}} dz = I_0 t^{\frac{2}{3}} \sim t^{\frac{2}{3}}, \quad (\text{B.8})$$

where $I_0 = 2\pi \int_{-\infty}^{\infty} (G^2 + \mathcal{K}zG) (\mathcal{A}_{\text{disp}} + z) dz$. Similarly, Eq. (13) yields for the mass of the product,

$$M_C \sim t^{\frac{5}{3}}. \quad (\text{B.9})$$

Finally, using Eq. (10), we deduce that the reaction front width scales as

$$w_f \sim t^\alpha = t^{\frac{1}{3}} \quad (\text{B.10})$$

Appendix B.2. The dispersion-dominated mixing-limited sub-regime ($t \gg 1$ and $r_f \ll \eta Pe$)

At moderately large times, i.e., for $t \gg 1$ but before the transition into the diffusion-dominated regime occurs (see the inference (iii) in §3.2), the presence of mechanical dispersion may lead to a second novel transport regime. This regime is realized when $\eta Pe \gg 1$ (based on the definition of $t_{\text{tr}}^{\text{diff}}$, see §3.2.3.2), such that the front location satisfies $r_f \ll \eta Pe$ even when $t \gg 1$. At the same time, if $\eta \gg 1$ (based on the definition of $t_{\text{tr}}^{\text{disp}}$, see §3.2.3.2), it becomes possible to deduce analytical scaling estimates for the reaction front properties for the interval $1 \leq t \leq \eta^2$, as outlined below. We deduce in §Appendix C.2 that for Eq. (B.5) to remain physically consistent in $t \gg 1$, one must have $\alpha = 0$ (leading to $\beta = 2/3$). As a result, Eq. (B.5) reduces to, $d_z^2 G + (1 - Pe)/(\eta Pe) d_z G - (\mathcal{A}_{\text{disp}}/\eta) (G^2 + \mathcal{K}zG) = 0$, and using Eq. (B.6), we deduce,

$$\bar{R} \sim t^{-\frac{1}{3}}. \quad (\text{B.11})$$

The product mass (Eq. (13)) is then given by,

$$M_C \sim t^{\frac{2}{3}}. \quad (\text{B.12})$$

Finally, using Eq. (10), the reaction front width scales as,

$$w_f \sim t^\alpha = t^0. \quad (\text{B.13})$$

Appendix B.3. The diffusion-dominated reaction-limited sub-regime ($t \ll 1$ and $r_f \gg \eta Pe$)

In case of weak mechanical dispersion ($\eta \ll 1$), if the condition $r_f \gg \eta Pe$ is satisfied at early times, i.e., for $t \ll 1$, the front will transition into a diffusion-dominated regime before the reaction front becomes mixing-limited. As a result, it may be shown (see [Appendix C.3](#)) that a physically and mathematically consistent form of Eq. (B.5) requires, $\alpha = 1/2$ (giving us $\beta = 0$) and as a result the same simplifies to: $(\mathcal{A}_{\text{diff}} + z) d_z^2 G + [(1 - Pe) + Pe (\mathcal{A}_{\text{diff}} z + z^2)/2] d_z G = 0$. It then follows from Eq. (B.6) that:

$$\bar{R} \sim t. \quad (\text{B.14})$$

The mass of the product (Eq. (13)) and front width (Eq. (10)) are given by:

$$M_C \sim t^2, \text{ and } w_f \sim t^\alpha = t^{\frac{1}{2}}. \quad (\text{B.15})$$

Appendix B.4. The diffusion-dominated mixing-limited sub-regime ($t \gg 1$ and $r_f \gg \eta Pe$)

As noted earlier, at sufficiently large times ($t \gg 1$), $r_f \gg \eta Pe$ must be satisfied regardless of how strong dispersion is. At this stage, it may be shown that $\alpha = 1/6$ (giving us $\beta = 2/3$) is required for a consistent form of Eq. (B.5) (see the work of [Braun et al. \(2017\)](#) and [Appendix C.4](#)). Hence, this equation simplifies to $d_z^2 G - Pe (G^2 + \mathcal{K} z G) = 0$. Using Eq. (B.6), we then deduce

$$\bar{R} \sim t^0. \quad (\text{B.16})$$

The product mass (Eq. (13)) and the front width (Eq. (10)) scale as,

$$M_C \sim t, \text{ and } w_f \sim t^\alpha \sim t^{\frac{1}{6}}. \quad (\text{B.17})$$

Appendix C. Brief derivation of the values of α appearing in §3.2.1, §3.2.2 and Appendix B

Appendix C.1. The early time dispersion-dominated reaction-limited sub-regime

Proceeding with Eq. (B.5) in the dispersion-dominated regime, we emphasize that early time implies $t \ll 1$. For this, we identify the prospective intervals for α as: (i) $\alpha < -2/3$, (ii) $-2/3 \leq \alpha < 0$, (iii) $0 \leq \alpha < 1/3$ and (iv) $\alpha \geq 1/3$. These values are identified such that Eq. (B.5) shows distinct behavior in each of these intervals, when attempting to fulfil the following requirements: (a) None of the terms in Eq. (B.5) should have a negative power of t ; and (b) The second derivative term $d_z^2 G$ must be retained (otherwise the nature of the equation changes). These requirements

ensure that Eq. (B.5) remains physically and mathematically consistent. For (i) $\alpha < -2/3$ and (ii) $-2/3 \leq \alpha < 0$, the above requirements cannot be simultaneously fulfilled whilst also restricting α within the respective intervals. When the intervals (iii) $0 \leq \alpha < 1/3$ and (iv) $\alpha \geq 1/3$ are chosen, in both cases we estimate $\alpha = 1/3$, which falls outside interval (iii), but inside interval (iv). Therefore, $\alpha = 1/3$ stands out as the deduced value of α in the early time dispersion-dominated reaction-limited sub-regime.

Appendix C.2. The dispersion-dominated mixing-limited sub-regime at moderately large times

We again start with Eq. (B.5) in the dispersion-dominated regimes, and emphasize that the moderately large time regime implies $t \gg 1$. For this also, the prospective intervals for α are the same as listed in §Appendix C.1. A physically and mathematically consistent form of Eq. (B.5) now requires that: (a) none of the terms in Eq. (B.5) should have a positive power of t , along with the requirement (b) as stated in §Appendix C.1. For the intervals (i) $\alpha < -2/3$ and (iv) $\alpha \geq 1/3$, the above requirements cannot be simultaneously satisfied whilst restricting α within the respective interval. On the other hand, the intervals (ii) $-2/3 \leq \alpha < 0$ and (iii) $0 \leq \alpha < 1/3$ both lead to $\alpha = 0$, which falls outside the interval (iii), but within the interval (iv). Therefore, $\alpha = 0$ stands out as the deduced value of α during the dispersion-dominated mixing-limited sub-regime at moderately large times.

Appendix C.3. The diffusion-dominated reaction-limited sub-regime

Proceeding with Eq. (B.5) in the diffusion-dominated regime, we recall that the early time implies $t \ll 1$. The conditions ensuring the physical and mathematical consistency of Eq. (B.5) remain identical to those in Appendix C.1, while the prospective intervals for α now are: (i) $\alpha < -1/2$, (ii) $-1/2 \leq \alpha < 1/2$ and (iii) $\alpha \geq 1/2$. Following the same line of reasoning as outlined in Appendix C.1, the value of α is deduced as $\alpha = 1/2$ in the interval (iii).

Appendix C.4. The diffusion-dominated mixing-limited sub-regime at large times

We again start with Eq. (B.5) in the diffusion-dominated regime and note that in the large time, $t \gg 1$. The conditions ensuring the physical and mathematical consistency of Eq. (B.5) remain identical to those in Appendix C.2, while the prospective intervals for α are identical to those in Appendix C.3. Following the same line of reasoning as outlined in Appendix C.2, the value of α is deduced as $\alpha = 1/6$ in the interval (ii).

References

- Addassi, M., Omar, A., Hoteit, H., Afifi, A.M., Arkadakskiy, S., Ahmed, Z.T., Kunnummal, N., Gislason, S.R., Oelkers, E.H., 2022. Assessing the potential of solubility trapping in unconfined aquifers for subsurface carbon storage. *Sci. Rep.* 12, 20452.
- Arshadi, M., Rajaram, H., 2019. Transport with bimolecular reactions in a fracture-matrix system: Analytical solutions with applications to in situ chemical oxidation. *Water Resour. Res.* 55, 3904–3924.
- Bandopadhyay, A., Le Borgne, T., Méheust, Y., Dentz, M., 2017. Enhanced reaction kinetics and reactive mixing scale dynamics in mixing fronts under shear flow for arbitrary damköhler numbers. *Advances in water resources* 100, 78–95.
- Batareseh, K.I., Stiller, A.H., 1994. Modeling the role of bacteria in leaching of low-grade ores. *AIChE J.* 40, 1741–1756.
- Bear, J., 2018. Modeling phenomena of flow and transport in porous media. volume 1. Springer.
- Berkowitz, B., Cortis, A., Dentz, M., Scher, H., 2006. Modeling non-fickian transport in geological formations as a continuous time random walk. *Rev. Geophys.* 44.
- Bochet, O., Bethencourt, L., Dufresne, A., Farasin, J., Pédro, M., Labasque, T., Chatton, E., Lavenant, N., Petton, C., Abbott, B.W., et al., 2020. Iron-oxidizer hotspots formed by intermittent oxic–anoxic fluid mixing in fractured rocks. *Nature Geoscience* 13, 149–155.
- Brau, F., De Wit, A., 2020. Influence of rectilinear vs radial advection on the yield of $a + b \rightarrow c$ reaction fronts: A comparison. *J. Chem. Phys.* 152, 054716.
- Brau, F., Schuszter, G., De Wit, A., 2017. Flow control of $a + b \rightarrow c$ fronts by radial injection. *Phys. Rev. Lett.* 118, 134101.
- Budroni, M., Upadhyay, V., Rongy, L., 2019. Making a simple $a + b \rightarrow c$ reaction oscillate by coupling to hydrodynamic effect. *Phys. Rev. Lett.* 122, 244502.
- Burté, L., Cravotta III, C.A., Bethencourt, L., Farasin, J., Pédro, M., Dufresne, A., Gérard, M.F., Baranger, C., Le Borgne, T., Aquilina, L., 2019. Kinetic study on clogging of a geothermal

pumping well triggered by mixing-induced biogeochemical reactions. *Environmental science & technology* 53, 5848–5857.

Comolli, A., De Wit, A., Brau, F., 2019. Dynamics of $a + b \rightarrow c$ reaction fronts under radial advection in three dimensions. *Phys. Rev. E* 100, 052213.

Comolli, A., De Wit, A., Brau, F., 2021. Dynamics of $a + b \rightarrow c$ reaction fronts under radial advection in a poiseuille flow. *Phys. Rev. E* 104, 044206.

Copley, S.D., 2009. Evolution of efficient pathways for degradation of anthropogenic chemicals. *Nat. Chem. Biol.* 5, 559–566.

De Anna, P., Dentz, M., Tartakovsky, A., Le Borgne, T., 2014. The filamentary structure of mixing fronts and its control on reaction kinetics in porous media flows. *Geophys. Res. Lett.* 41, 4586–4593.

De Anna, P., Le Borgne, T., Dentz, M., Tartakovsky, A.M., Bolster, D., Davy, P., 2013. Flow intermittency, dispersion, and correlated continuous time random walks in porous media. *Phys. Rev. Lett.* 110, 184502.

Dentz, M., Le Borgne, T., Englert, A., Bijeljic, B., 2011. Mixing, spreading and reaction in heterogeneous media: A brief review. *J. Contam. Hydrol.* 120, 1–17.

Edery, Y., Scher, H., Berkowitz, B., 2009. Modeling bimolecular reactions and transport in porous media. *Geophys. Res. Lett.* 36.

Eldor, M., Dagan, G., 1972. Solutions of hydrodynamic dispersion in porous media. *Water Resour. Res.* 8, 1316–1331.

Gálfi, L., Rácz, Z., 1988. Properties of the reaction front in an $a + b \rightarrow c$ type reaction-diffusion process. *Phys. Rev. A* 38, 3151.

Gautam, K., Narayana, P., 2019. On the stability of carbon sequestration in an anisotropic horizontal porous layer with a first-order chemical reaction. *Proceedings of the Royal Society A* 475, 20180365.

Ghosh, U., Borgne, T., Jougnot, D., Linde, N., Méheust, Y., 2018. Geoelectrical signatures of reactive mixing: a theoretical assessment. *Geophys. Res. Lett.* 45, 3489–3498.

- Guilbert, E., Almarcha, C., Villiermaux, E., 2021. Chemical reaction for mixing studies. *Phys. Rev. Fluids* 6, 114501.
- Guyon, E., Hulin, J.P., Petit, L., Mitescu, C.D., 2015. *Physical hydrodynamics*. Oxford university press.
- Haynes, W.M., Lide, D.R., Bruno, T.J., 2016. *CRC handbook of chemistry and physics*. CRC press.
- Jiménez-Martínez, J., Anna, P.d., Tabuteau, H., Turuban, R., Borgne, T.L., Méheust, Y., 2015. Pore-scale mechanisms for the enhancement of mixing in unsaturated porous media and implications for chemical reactions. *Geophys. Res. Lett.* 42, 5316–5324.
- Larralde, H., Araujo, M., Havlin, S., Stanley, H.E., 1992. Reaction front for $a+b \rightarrow c$ diffusion-reaction systems with initially separated reactants. *Phys. Rev. A* 46, 855.
- Le Borgne, T., Dentz, M., Villiermaux, E., 2015. The lamellar description of mixing in porous media. *J. Fluid Mech.* 770, 458–498.
- Le Borgne, T., Ginn, T.R., Dentz, M., 2014. Impact of fluid deformation on mixing-induced chemical reactions in heterogeneous flows. *Geophys. Res. Lett.* 41, 7898–7906.
- Leal, L.G., 2007. *Advanced transport phenomena: fluid mechanics and convective transport processes*. volume 7. Cambridge University Press.
- Levy, M., Berkowitz, B., 2003. Measurement and analysis of non-fickian dispersion in heterogeneous porous media. *J. Contam. Hydrol.* 64, 203–226.
- Liu, N., Wu, L., Qin, Z., Shoesmith, D.W., 2016. Roles of radiolytic and externally generated h_2 in the corrosion of fractured spent nuclear fuel. *Environ. Sci. Technol.* 50, 12348–12355.
- Luo, J., Dentz, M., Carrera, J., Kitanidis, P., 2008. Effective reaction parameters for mixing controlled reactions in heterogeneous media. *Water Resour. Res.* 44.
- Maliva, R.G., Maliva, R.G., 2020. *Anthropogenic aquifer recharge and water quality*. Springer.
- Miller, P., Vasudevan, D., Gschwend, P., Roberts, A., 1998. Transformation of hexachloroethane in a sulfidic natural water. *Environ. Sci. Technol.* 32, 1269–1275.

- Narr, W., 1996. Estimating average fracture spacing in subsurface rock. *AAPG Bull.* 80, 1565–1585.
- Neuman, S.P., Tartakovsky, D.M., 2009. Perspective on theories of non-fickian transport in heterogeneous media. *Advances in Water Resources* 32, 670–680.
- Neupauer, R.M., Sather, L.J., Mays, D.C., Crimaldi, J.P., Roth, E.J., 2020. Contributions of pore-scale mixing and mechanical dispersion to reaction during active spreading by radial groundwater flow. *Water Resour. Res.* 56, e2019WR026276.
- Noettinger, B., Roubinet, D., Russian, A., Le Borgne, T., Delay, F., Dentz, M., De Dreuzy, J.R., Gouze, P., 2016. Random walk methods for modeling hydrodynamic transport in porous and fractured media from pore to reservoir scale. *Transp. Porous Media* 115, 345–385.
- Olver, F.W., Lozier, D.W., Boisvert, R.F., Clark, C.W., 2010. *NIST handbook of mathematical functions* hardback and CD-ROM. Cambridge university press.
- Patankar, S.V., 2018. *Numerical heat transfer and fluid flow*. CRC press.
- Patil, D., Sharma, A., 2011. Study on the corrosion kinetics of iron in acid and base medium. *E-J. Chem.* 8, S358–S362.
- Phenrat, T., Lowry, G.V., 2019. *Nanoscale zerovalent iron particles for environmental restoration. From Fundamental Science to Field Scale Engineering Applications*.
- Rolle, M., Le Borgne, T., 2019. Mixing and reactive fronts in the subsurface. *Rev. Mineral. Geochem.* 85, 111–142.
- Rossi, F., Cucciniello, R., Intiso, A., Proto, A., Motta, O., Marchettini, N., 2015. Determination of the trichloroethylene diffusion coefficient in water. *AIChE J.* 61, 3511–3515.
- Saffman, P., 1959. A theory of dispersion in a porous medium. *J. Fluid Mech.* 6, 321–349.
- Saripalli, K., Sharma, M., Bryant, S., 2000. Modeling injection well performance during deep-well injection of liquid wastes. *J. Hydrol.* 227, 41–55.
- Sprocati, R., Rolle, M., 2020. Charge interactions, reaction kinetics and dimensionality effects on electrokinetic remediation: A model-based analysis. *J. Contam. Hydrol.* 229, 103567.

- Stolze, L., Rolle, M., 2022. Surface complexation reactions in sandy porous media: Effects of incomplete mixing and mass-transfer limitations in flow-through systems. *J. Contam. Hydrol.* 246, 103965.
- Sundstrom, D., Klei, H., Nalette, T., Reidy, D., Weir, B., 1986. Destruction of halogenated aliphatics by ultraviolet catalyzed oxidation with hydrogen peroxide. *Hazard. Waste Hazard. Mater.* 3, 101–110.
- Valocchi, A.J., Bolster, D., Werth, C.J., 2019. Mixing-limited reactions in porous media. *Transport in Porous Media* 130, 157–182.
- Wang, Q., Gu, H., Zhan, H., Shi, W., Zhou, R., 2020. Mixing effect on reactive transport in a column with scale dependent dispersion. *J. Hydrology* 582, 124494.
- Wing, M.R., 1997. Apparent first-order kinetics in the transformation of 1, 1, 1-trichloroethane in groundwater following a transient release. *Chemosphere* 34, 771–781.
- Zhang, W.x., 2003. Nanoscale iron particles for environmental remediation: an overview. *J. Nanopart. Res.* 5, 323–332.

Author Statement (Manuscript No. ADWR-D-23-00314)

PK: Methodology, Formal analysis, Writing - original draft, Funding acquisition; **UG:** Conceptualization, Methodology, Resources, Writing - review and editing, Supervision, Funding acquisition; **YM:** Conceptualization, Writing-review and editing, Supervision; **TLB:** Conceptualization, Writing-review and editing, Supervision

Declaration of interests

☒ The authors declare that they have no known competing financial interests or personal relationships that could have appeared to influence the work reported in this paper.

☐ The authors declare the following financial interests/personal relationships which may be considered as potential competing interests: